Physics-Based Modeling of Hot-Carrier Degradation

Stanislav Tyaginov

Abstract We present and verify a physics-based model of hot-carrier degradation (HCD). This model is based on a thorough solution of the Boltzmann transport equation. Such a solution can be achieved using either a stochastic solver based on the Monte Carlo approach or a deterministic counterpart that is based on representation of the carrier energy distribution function as a series of spherical harmonics. We discuss and check two implementations of our model based on these methods. The model is verified vs. the HCD experimental data measured in long-channel transistors as well as in ultra-scaled MOSFETs. Because both stochastic and deterministic methods have advantages and shortcomings, we study the limits of applicability of these methods. We aim to cover and link all main features of HCD, namely, the interplay between hot and colder carriers, which leads to two competing mechanisms of bond breakage and the strong localization of hot-carrier damage. Our model is linked and compared with other approaches to HCD simulations. Special attention is paid to the importance of the particular model ingredients, such as competing mechanisms of the Si–H bond dissociation, electron–electron scattering, variations in the bond-breakage energy, as well as its reduction due to the interaction between the dipole moment of the bond and the electric field. We also analyze the role of electron–electron scattering in HCD measured in devices with different gate lengths.

1 Introduction

If a voltage between the source and the drain of the MOSFET is applied, the charge carriers are accelerated by the electric field and can gain substantially high energies, depending on the applied bias. When such carriers interact with the insulator–silicon interface of the MOSFET, they deposit energy, thereby producing damage at or near this interface; see Fig. 1. This detrimental effect is called "hot-carrier degradation" (HCD) and was initially reported in the early 1970s [1]. The term "hot" suggests that

S. Tyaginov (✉)
Institute for Microelectronics, Technische Universität Wien,
Gusshausstrasse 27-29/E360, Wien, Austria
e-mail: tyaginov@iue.tuwien.ac.at
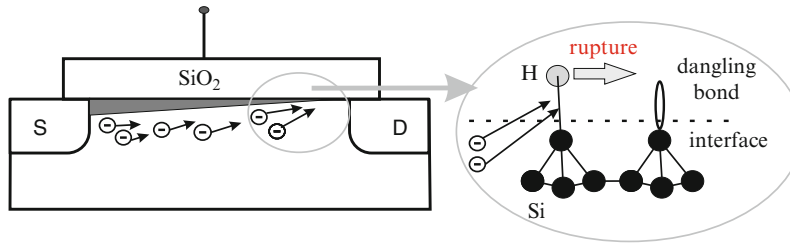
Fig. 1 A schematic representation of hot-carrier degradation. Carriers colliding the dielectric/Si interface in a MOSFET can deposit their energy, thereby producing damage. This damage is associated with dissociation of Si–H bonds. If such a bond is broken, a dandling bond remains. This dangling bond is electrically active, can trap electrons/holes, become charged, and hence distort the electrostatics of the device and aggravate the carrier mobility

Fig. 2 The dangling Si–bond at the Si/SiO_2 interface and the passivated Si–H bond. Hydrogen incorporated into the device terminates at an electrically active dangling Si– bond, thereby converting it into a Si–H bond
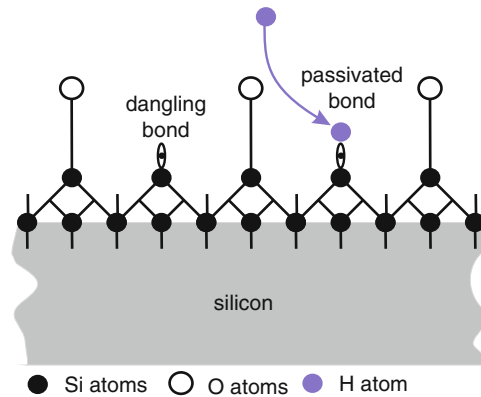
carriers triggering this process are severely non-equilibrium and are characterized by high energies. This was the case at the time of pioneering works devoted to HCD [1–3] when the transistor operating voltages were high enough to ensure these energies. However, the situation has changed with the aggressive MOSFET scaling, and now channel cold carriers can also contribute to HCD [4, 5].

It is widely adopted that hot-carrier damage is due to dissociation of Si–H bonds at the interface, which is triggered by channel carriers. In fact, the modern CMOS technology demands an annealing step, which follows the dielectric film growth. This is because silicon dioxide employed as the gate dielectric in almost all MOSFETs (even in novel high-*k*/metal gate stacks, an interfacial SiO_2 layer is needed) is of amorphous nature. The structural disorder at this interface results in—among other things—dangling silicon bonds (see Fig. 2). These dangling bonds are electrically active and can capture charge carriers. To passivate them, hydrogen species are intentionally incorporated in the device. Hydrogen terminates these dangling bonds, thereby forming passive Si–H bonds. If then a Si–H bond is dissociated due to the interaction with the packet of channel carriers, this process

results again in a dangling Si– bond. This dangling bond can capture a carrier, become charge, and therefore locally perturb the device electrostatics and degrade the mobility.

The Si–H bond-bonding energy was reported to be above 1.5 eV [5, 6]. At the same time, the rapid MOSFET miniaturization has resulted in operating voltages as low as ∼1 V, thereby making hot electrons unlikely in these devices. As a result, it was expected that HCD would be severely suppressed or totally removed in such scaled transistors. This idea, however, was dispelled, for example, in the paper by Mizuno et al. [4], where a transistor was subjected to hot-carrier stress at the drain voltage of less than 1 V and a substantial change of the device characteristics was observed. As a consequence, the HCD paradigm has been extended in order to include the contribution of "cold" carriers into consideration [5, 7, 8]. These cold carriers were shown to contribute to the entire bond-breakage process due to two main reasons.

First, scattering mechanisms can exchange carrier energy in a fashion to populate the high-energy fraction of the carrier ensemble, thereby triggering HCD even if the stress/operating voltage is below 1 V [8–13]. Second, in scaled devices, the dominant mechanism of Si–H bond dissociation is based on the multiple vibrational excitation (MVE) of the bond, which is triggered by a series of cold carriers [7, 14–16]. This is in contrast to long-channel devices, where the bond dissociation event can be induced by a solitary hot carrier in a single collision [7, 14–16]. In recent papers on HCD, however, it has been shown that under real operating conditions, intricate combinations of these processes can be realized in short- and long-channel MOSFETs [17–20].

The rates of both scattering and bond-breakage mechanisms are determined by the manner in which the particles in the carrier ensemble are distributed over energy. Mathematically, this means that the proper modeling of HCD needs to be based on the carrier energy distribution function (DF). This DF can be obtained as a solution of the Boltzmann transport equation (BTE). Such a solution is demanding and needs substantial computational resources [21, 22]. This is the reason why in most of the physical HCD models, this thorough BTE solution is avoided. For instance, one of the most successful HCD models developed by Bravaix group [5, 23, 24] is based on the so-called energy-driven paradigm proposed by Rauch and La Rosa, see [25, 26] and the chapter in this book [27]. According to this paradigm, the bond-breakage rate is determined by some "knee" energies, which are related to stress/operating conditions. As a result, a challenging evaluation of the carrier DF is eliminated and the bond-breakage rates are modeled using some empirical parameters. In the same spirit, the early version of the Bravaix model considers scattering and bond-breakage mechanisms as independent processes and their rates are linked to some phenomenological/fitting factors [5, 23].

This treatment, however, appears doubtful because scattering mechanisms and bond-breakage processes affect each other via the carrier distribution over energy. For instance, traps generated during hot-carrier stress can capture electrons. As a result, they act as additional scattering centers and also perturb the local potential. Hence, the carrier DF is affected due to the bond-rupture process, and the scattering

mechanism rates—which, vice versa, control the DF—are also impacted. To conclude, the energy exchange mechanisms and bond dissociation processes need to be considered self-consistently within the same simulation framework. The first realization of such a self-consistent consideration has recently been proposed within the latest version of the Bravaix model; see [24, 28].

We present and verify a physical HCD model that is based on a thorough BTE solution. The model consolidates three components essential for a proper description of HCD: (1) Boltzmann transport equation solver, which allows (2) proper treatment of the bond-breakage kinetics and (3) simulation of the degraded devices. To solve the BTE, we use a stochastic solver based on the Monte Carlo (MC) method and a deterministic solver that employs the spherical harmonics expansion (SHE) of the carrier DF. Both versions of the model will be verified against the experimental data that were measured on both ultra-scaled and long-channel devices. Finally, we comment on the vitality of each of the model versions and analyze the importance of different model ingredients.

2   Main Peculiarities of Hot-Carrier Degradation

One of the main features of HCD is its strong localization [29–31]. Indeed, the electric field accelerates electrons from the source to the drain (see Fig. 3). Thereby, the group velocity of the carrier packet increases from the source to the drain. Near the drain, hot-channel electrons mix with the thermalized carriers of the drain, and thus the average carrier energy is again close to the equilibrium one. Therefore, the maximum carrier energy is observed near the drain end of the gate (see Fig. 4). At the same time, the peak of the electric field is also usually situated between the gate and the drain (Fig. 4). Note also that the carrier energy is gained from the electric field, which is responsible for the carrier acceleration.
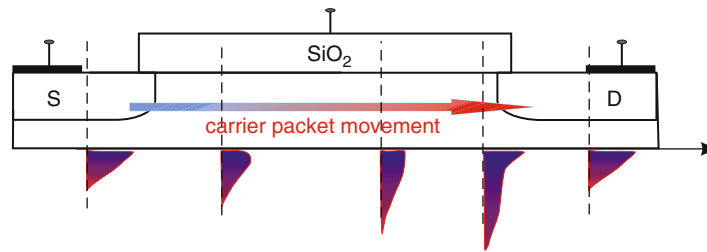
Fig. 3 A schematic representation of the carrier DF evolution while the carrier packet moves from the source to the drain. Near the source, electrons are in equilibrium and obey a Maxwell distribution. In the center of the device and near the drain end of the gate, they are severely non-equilibrium. Penetrating the drain p-n junction, hot electrons mix with the thermalized carriers of the drain, and thus their average energy drops to the equilibrium value
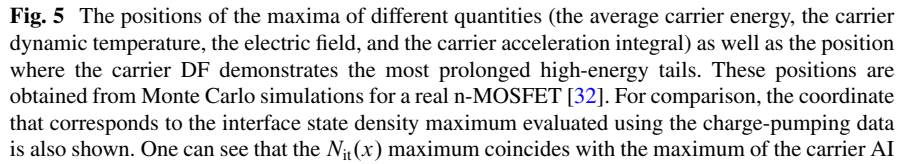
Fig. 4 A schematic representation of lateral profiles of different quantities that can be considered the driving force of HCD (the electric field and the average carrier energy) as well as the interface state density $N_{it}(x)$ as a function of the coordinate along the interface. One can see that all three quantities have maxima near the drain end of the gate
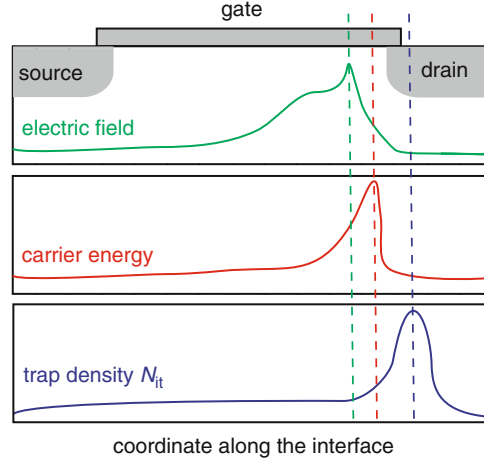
All these considerations complicate the matter and result in two competing concepts of understanding the HCD phenomenon: (1) HCD is field-driven vs. (2) hot-carrier damage is triggered by energy deposited by carriers. The first concept resulted in one of the most popular HCD models, namely, the so-called lucky electron model proposed by Hu [3]. Within this paradigm, it is assumed that an electron has high enough energy to overcome the potential barrier at the Si/SiO_2 interface without energy loss and without being scattered back into the channel. This electron ends up in the SiO_2 conduction band, deposits its excessive energy, and therefore produces a defect. The energy of this lucky electron is obtained from the electric field, and the electric field is the driving force of HCD.

Later, however, the IBM group had performed a series of different hot-carrier stresses using different injection modes, namely, Fowler–Nordheim and direct tunneling stresses as well as substrate hot-carrier and channel hot-carrier stress. In a series of papers [33–35], it was shown that the interface state generation probability depends only on the maximum energy deposited by carriers, not on the electric field, and is insensitive to the concrete stress mechanism. These findings have led to the energy-driven paradigm of HCD [25, 26]. Therefore, many of the early empirical and/or phenomenological HCD models linked the interface state generation rate with one of the macroscopic quantities, such as the electric field, average carrier density, or dynamic temperature (Fig. 4). In our recent papers [32, 36], however, it was shown that the peak of the interface state concentration N_{it} does not coincide with any of these quantities and is better described by the carrier acceleration integral (AI), which represents the cumulative ability of the carrier ensemble to dissociate the bonds and will be introduced in Sect. 3 (see Fig. 5).

For a full understanding of HCD, we need to respond to an important question: Why can HCD still be severe even in ultra-scaled devices with operating voltages of $\sim$1 V and below where hot carriers are unlikely? One of the main reasons for this is the energy exchange mechanisms populating the hot-carrier fraction of the ensemble

Fig. 5 The positions of the maxima of different quantities (the average carrier energy, the carrier dynamic temperature, the electric field, and the carrier acceleration integral) as well as the position where the carrier DF demonstrates the most prolonged high-energy tails. These positions are obtained from Monte Carlo simulations for a real n-MOSFET [32]. For comparison, the coordinate that corresponds to the interface state density maximum evaluated using the charge-pumping data is also shown. One can see that the $N_{it}(x)$ maximum coincides with the maximum of the carrier AI

[8–13]. Among these mechanisms are impact ionization, Auger recombination, electron–phonon, and electron–electron scattering. Another important ingredient is the bond dissociation mechanism, which is triggered by the multiple vibrational excitation of the bond induced by a series of colder carriers.

We start with the Si–H bond dissociation process based on the MVE process that is dominant in ultra-scaled MOSFETs. In other words, the process driving hot-carrier degradation changes when the device dimensions shrink. In fact, in the 1980s, device operating voltages were high and carriers with energies above 1.5 eV (above the threshold of the bond dissociation reaction) were presented in substantial quantities. Such an energetic carrier can trigger the bond dissociation process in a single collision, and this process is therefore called a "single-particle" (SP) mechanism (see Fig. 6). Due to the huge disparity between the electron mass and the mass of the hydrogen nucleus and conservation of the total momentum of the system, the energy portion transferred to the bond in a direct collision is negligibly small and cannot provoke bond dissociation. Instead, one of the bonding electrons is excited to an antibonding (AB) state [37]. This induces a repulsive force that acts on the H atom and results in its release.

In ultra-scaled MOSFETs, however, operating voltages are much lower and can be below 1 eV. Therefore, the probability that the ensemble contains these high-energy carriers is rather low and the SP mechanism is characterized by a very
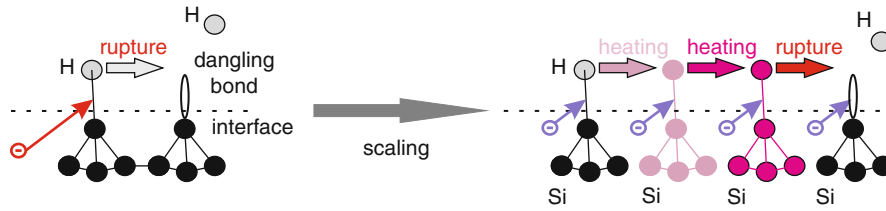
Fig. 6 The change of the dominant mechanism of Si–H bond dissociation from the single-particle to the multiple-particle process. This change accompanies the device miniaturization. If the stress/operating bias is high enough, carriers are hot and induce the bond dissociation event in a single collision (SP mechanism). In contrast, in ultra-scaled devices, these carriers do not present in sufficient quantities. Instead, the bond can be dissociated by a series of colder carriers that induce the multiple vibrational dissociation of the bond (the MP process)

low rate. Instead, dissociation can be triggered by a series of colder carriers that subsequently bombard the interface. These carriers can induce the MVE of the bond. When the bond is situated on the highest bonded state, only a small portion of energy is required to trigger the hydrogen release event. This process is therefore called a "multiple-particle" (MP) mechanism.

On the device level, the change of the bond-breakage mechanism leads to the change of the worst-case HCD conditions when the device dimensions shrink. In long-channel devices, these conditions correspond to the maximum average energy of the carriers. In n-MOSFETs, the substrate current I_{sub} is often used as a criterion of HCD severity. This current I_{sub} consists of majority carriers generated by impact ionization, separated by the electric field from the minority carriers and collected by the bulk electrode. Both impact ionization and the bond dissociation process are adopted to have Keldysh-like reaction cross sections and the same structure of the rates [7, 26, 38]. Hence, I_{sub} can be used to judge on the impact ionization and bond dissociation intensities. The worst-case scenario is usually realized at $V_{gs} = (0.4$–$0.5)V_{ds}$. Due to the same reasons, in p-MOSFETs, HCD worst-case conditions correspond to the gate current maximum, but such an empirical interrelation between V_{gs} and V_{ds} is not established [8, 15, 16]. In ultra-scaled devices, however, the maximum average energy is not so important in the context of the HCD worst-case conditions. Rather, the carrier flux impinging on the interface plays a crucial role [8,15,16,39–41]. For both n- and p-channel ultra-scaled MOSFETs, the worst-case situation is realized when $V_{gs} \sim V_{ds}$.

As for the energy exchange mechanisms, in long-channel devices they usually suppress the high-energy fraction of the ensemble, thereby softening HCD. In ultra-scaled MOSFETs, however, they can reinforce HCD or even be responsible for it. The common action of different scattering mechanisms determines the temperature behavior of HCD. In contrast to the sister phenomenon of bias temperature instability, which becomes more severe at higher temperatures, the situation with HCD is more complicated. In long-channel devices, HCD was shown to be suppressed if the temperature increases [42]. This can be explained in terms of the rates of
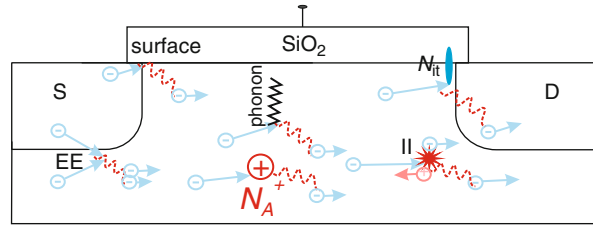
Fig. 7 A schematic representation of main carrier exchange mechanisms: impact ionization; scattering at ionized impurities; surface scattering; electron–electron and electron–phonon scattering. If interface traps are generated during stress, they can capture charge carriers and act as additional scattering centers, therefore degrading the mobility
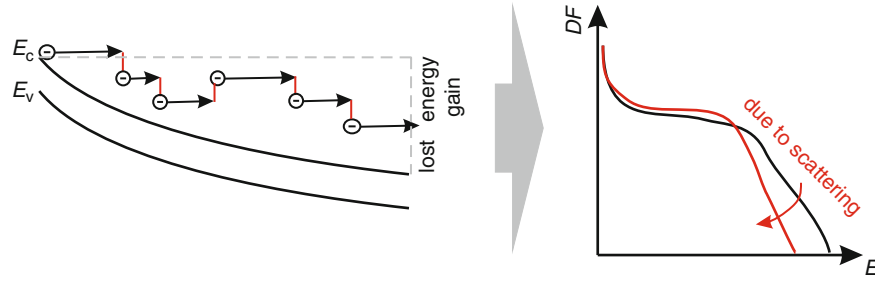

Fig. 8 Energy exchange mechanisms usually lead to energy loss. Thus, without scattering mechanisms, carriers would have gained higher energy from the electric field (determined by the applied bias), left panel. In terms of the carrier energy DF, this means that the high-energy tail of the DF is suppressed, right panel

the scattering mechanisms (see Fig. 7). While moving through the device, carriers undergo scattering events, thereby exchanging their energy. This results in evolution of the carrier DF while the carrier packet drives from the source to the drain (see Fig. 3). Five main scattering mechanisms affect the DF: impact ionization; surface scattering; scattering at ionized impurities; electron–phonon and electron–electron scattering. Note that charged defects created during stress also act as scattering centers and can substantially affect the carrier energy distribution. Distortion of the carrier DF is usually related to depopulation of the high-energy fraction of the carrier ensemble (see Fig. 8). The scattering mechanism rates increase with temperature, and therefore depopulation of the hot fraction of the ensemble becomes more efficient. As a result, sweeping out of hot carriers leads to suppression of HCD in long-channel devices, where HCD is dominated by the SP mechanism.

In ultra-scaled MOSFETs, however, electron–electron scattering (EES) plays a crucial role [9, 10, 38, 43]. EES can populate the high-energy tail of the carrier DF and be responsible for pronounced HCD even if the stress/operating voltage is scaled below 1 V. This two-particle process was shown to convert a pair of two electrons with moderate energies into a pair where one of the carriers is cold while another one is hot, thereby contributing to the hot fraction of the ensemble
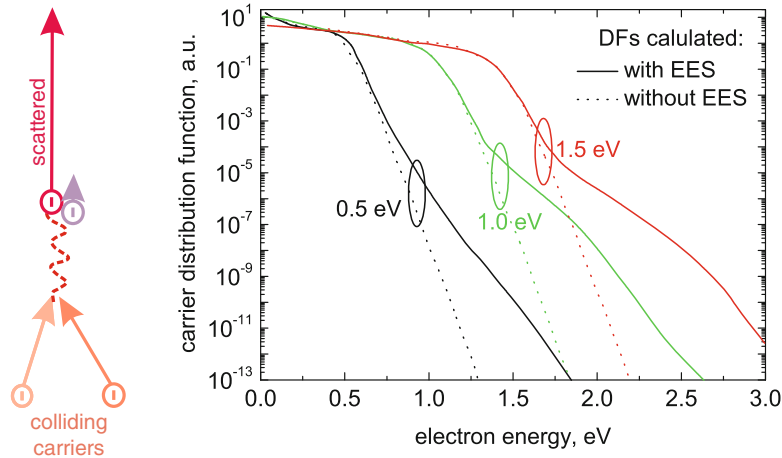
Fig. 9 EES can populate the high-energy tail of the carrier DF. This mechanism converts the carriers with moderate energies into a pair of electrons, where one of the carriers is cold while another one is hot, *right panel*. The effect of EES results in humps pronounced in high-energy tails of the carrier DF, *left panel* (adopted from [43])

(see Fig. 9). This results in characteristic humps pronounced in the DF high-energy tails (Fig. 9). The key role of EES in short-channel MOSFETs leads to two important consequences: HCD is strongly reinforced due to the contribution of EES; and the temperature behavior is changed.

The latter means that in ultra-scaled MOSFETs, HCD becomes more severe at elevated temperatures. This can be understood assuming that if the channel length is just a few decades of nanometers, there are a handful of doping atoms and a limited number of Si atoms. At the same time, the electron mean free path can be comparable with the channel length, and therefore an electron can pass the channel without interacting with lattice atoms. In other words, in such small devices, all scattering mechanisms—except EES—have low rates. On the other hand, the carrier concentration in the channel can be substantially high, and thus the carriers do interact with each other. Therefore, EES appears to be the only energy exchange mechanism that is significantly efficient. The rate of this mechanism increases with temperature, thereby determining HCD reinforcement when the device is heated.

It is worth noting that other scattering mechanisms can also be responsible for HCD in scaled transistors. Thus, Bude et al. have demonstrated that impact ionization can induce the gate leakage in a 100-nm n-MOSFET. The gate current was used to judge whether or not carriers are hot because in that thick oxide film, tunneling of equilibrium carriers has a low probability and only hot carriers can contribute to the gate leakage. Another mechanism that was shown to populate the high-energy tail of the carrier DF is Auger recombination [44]. According to this process, two recombining carriers transfer their energy to the third particle, which contributes to the gate current. Also, an electron can gain energy from phonons if

the number of absorbed phonons exceeds the number of emitted ones [45]. In [45], a Monte Carlo approach was applied to model this scenario in an n-MOSFET with a 100-nm channel length and the carrier DFs were shown to propagate beyond energies available from the electric field.

To summarize, all these essential peculiarities of HCD suggest that the key information needed for an adequate physics-based modeling of this phenomenon is the information about the carrier energy DF. Indeed, the interaction of the scattering mechanisms can result in either HCD suppression or its reinforcement, depending on the device geometry. As an intimately related peculiarity, HCD temperature behavior is also controlled by these mechanisms and the particular device architecture. The situation is even more complicated because bond dissociation and scattering processes need to be considered self-consistently within the same simulation framework. This is because charged defects perturb the device electrostatics and scatter carriers, thereby distorting the carrier energy distribution function, and hence the rates of the bond-breakage processes. Therefore, according to our vision, a physics-based HCD model has to be based on the carrier transport kernel, which links the microscopic level of defect generation and the device physics level. For this kernel, we use a BTE solver, which provides the information on the carrier DF for a particular device topology and given stress/operating conditions.

3 Physics-Based Models

To date there are four main HCD models available: the Hess model, the energy-driven paradigm by Rauch and La Rosa, the Bravaix model, and our own model based on the thorough BTE solution. The main concept of the HCD modeling was first proposed within a series of papers published by the Hess group [7, 14, 37]. For instance, the idea that an HCD model should be essentially based on carrier transport treatment was first pronounced within the Hess model [7, 37]. Also, the Hess model employs both SP and MP mechanisms as well as their superpositions [7, 14] and links this concept to the giant isotope effect [46]. Another fruitful idea employed in this approach is that the activation energy of the bond dissociation is a fluctuating quantity [47, 48]. All these vital ingredients were later inherited by the model developed by Bravaix's group [5, 23, 49]; for more details, see [24]. However, in contrast to the Hess model, carrier transport treatment is omitted and the model is realized on the basis of the energy-driven paradigm developed by Rauch and LaRosa [25–27].

3.1 Hess Model

The main breakthrough of the Hess model in the area of HCD modeling and understanding is introduction of the carrier AI and the idea that HCD is better described by this quantity [7, 14, 37]. Note that earlier the main competing concepts

striving to describe HCD were energy-driven and field-driven paradigms. In contrast to these paradigms, the Hess model considers the cumulative impact of the entire carrier ensemble on the bond dissociation process, and the measure of this effect is the carrier AI. As a consequence, the Hess concept naturally incorporates and takes into account two limiting cases: bond breakage by a solitary high-energy carrier; and bond dissociation induced by subsequent bombardment of the bond by several less energetic particles. The rates of both SP and MP mechanisms are determined by the AI, which in both cases has the same functional form. As we discussed, the most probable way of bond dissociation in a single collision is via excitation of one of the bonding electrons to an anti-bonding state. For this case, we explicitly write out the AI:

$$R_{\mathrm{SP}} \sim \int_{E_{\mathrm{th}}}^{\infty} F(E)P(E)\sigma(E)\mathrm{d}E, \tag{1}$$

where $F(E)$ is the carrier flux, that is, the number of carriers impinging on the interface per unit area and per unit time, $\sigma(E)$ is the bond dissociation reaction cross section, while $P(E)$ the probability that such a reaction leads to H release. The integration is performed starting from the activation energy for bond breakage E_{th}. Note that the flux $F(E)$ is just the product of the carrier energy DF, density of states, and the carrier velocity.

The concept of the MVE of the bond was first developed in the context of hydrogen/deuterium desorption from the passivated Si surface [46, 50–52]. This desorption has been induced by electrons tunneling from an STM tip. Carrier energies were low, and therefore the desorption was triggered by an MP process. Intriguingly, the hydrogen desorption rate appeared to be more than three orders of magnitude higher than the deuterium desorption rate, and therefore this effect was called the "giant isotope effect."

To describe the MVE process, one usually uses the truncated harmonic oscillator model for the Si–H bond (see Fig. 10). This oscillator is characterized by the system of eigenstates in the corresponding quantum well. The carrier flux that collides with the interface can induce either phonon absorption or emission, that is, the bond excitation/deexcitation processes. Being heavily bombarded by the carriers, the bond "climbs" the ladder of the bonded states (Fig. 10). When the bond is situated on the highest bonded level, only a small portion of energy is required for hydrogen release from this level to the transport mode. The rates of the bond excitation/deexcitation processes are

$$P_{\mathrm{d}} \sim \int_{E_{\mathrm{th}}}^{\infty} I(E)\sigma_{\mathrm{ab}}(E)[1 - f_{\mathrm{ph}}(E - \hbar\omega)]\mathrm{d}E,$$

$$P_{\mathrm{u}} \sim \int_{E_{\mathrm{th}}}^{\infty} I(E)\sigma_{\mathrm{emi}}(E)[1 - f_{\mathrm{ph}}(E + \hbar\omega)]\mathrm{d}E, \tag{2}$$
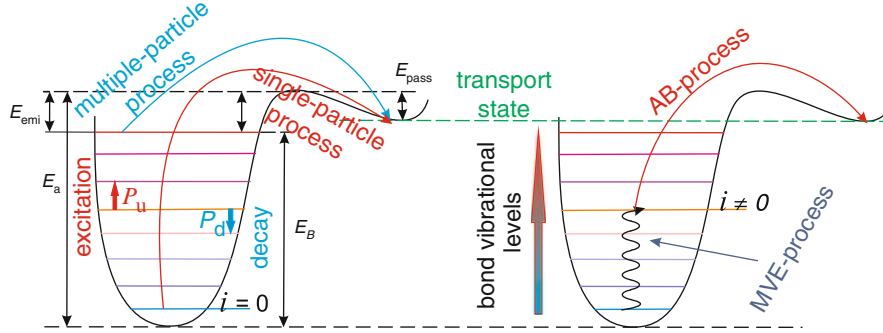
Fig. 10 A schematic representation of the Si–H bond within the truncated harmonic oscillator model. Bond dissociation can be triggered either by a solitary high-energy carrier or by a series of cold carriers. These mechanisms are termed "single-particle" and "multiple-particle" processes. Within the Hess model, the idea that the bond breakage can occur as a superposition of the MVE process (*right panel*) of the bond and hydrogen release induced by a single high-energy carrier (the AB mechanism) was first proposed

where $I(E)$ is the carrier flux bombarding the bond, σ_{ab} and σ_{emi} are the cross sections for the phonon absorption and emission reactions, respectively, and f_{ph} is the level occupation number, which obeys Bose–Einstein statistics. $\hbar\omega$ is the distance between the oscillator levels. Integration over energy is performed starting at the threshold energy E_{th} for this reaction. The rate of the MP process is then written as

$$R_{MP} = \left(\frac{E_B}{\hbar\omega} + 1\right)\left[P_d + \exp\left(\frac{-\hbar\omega}{k_B T_L}\right)\right]\left[\frac{P_u + \omega_e}{P_d + \exp(-\hbar\omega/k_B T_L)}\right]^{-E_B/\hbar\omega}, \quad (3)$$

where E_B is the energy level of the last bonded state, while ω_e is the reciprocal phonon lifetime, which defines the decay of the multiple vibrational modes.

Another pioneering idea formulated within the Hess model was the necessity to consider also the contributions of all the intermediate levels in the quantum well, not only the ground and last bonded states (see Fig. 10, right panel). First, the bond can be excited by subsequent bombardment by cold carriers to an intermediate level. Hydrogen release from this level requires much lower energy than that from the ground state, and therefore the probability of finding a solitary carrier with such an energy or above is substantially higher. In this case, the bond-breakage rate is

$$R = \sum_{i=0}^{N_l}\left[\frac{I_d f_v + \omega_e \exp\left(-\hbar\omega/k_B T_L\right)}{I_d f_v + \omega_e}\right]^i A^i I_d f_d. \quad (4)$$

Now the cumulative bond-breakage rate is linked to the drain current I_d via empirical factors A^i, f_d, and f_v. Each term in the sum of (4) represents the contribution of each particular level in the bond-breakage process. The prefactor in square brackets is just the ratio between rates P_u and P_d, which are now rewritten in a simplified manner and linked to the drain current:

$$P_u = I_d f_v + \omega_e,$$
$$P_d = I_d f_v + \omega_e exp\left(-\hbar\omega/k_B T_L\right). \tag{5}$$

SiO_2 is an amorphous material, and thus the Si/SiO_2 interface is characterized by disorder. This disorder leads to variations in the normally distributed activation energy, which obeys a Gaussian distribution. The normally distributed activation energy of the interface trap creation was observed experimentally [53–55] and confirmed by *ab initio* calculations. The dispersion of this energy has also been incorporated in the Hess model. For instance, two different power laws of degradation observed experimentally have been represented using this concept [48, 56]. One of the novel ideas associated with the Hess model is employment of the MVE concept in the context of HCD. The MVE concept was initially developed to describe H/D desorption from the Si surface but then has been successfully applied to model H release at the Si/SiO_2 interface. Another pioneering idea proposed by Hess group is a consequence of the giant isotope effect. The idea is to use deuterium instead of hydrogen while passivating the dangling bonds at the Si/SiO_2 interface [46]. The authors investigated the post-stress behavior of MOSFETs with hydrogen- and deuterium-annealed interfaces and demonstrated that the latter devices are more robust with respect to hot-carrier stress.

Although the Hess model is famous due to the pioneering concepts proposed, there are several shortcomings. The first is that the interface traps are considered at the microscopic level, which is not connected to the device level. Within the Hess model, the device lifetime is estimated as the time when the concentration N_{it} reaches a certain threshold. This estimation can lead to spurious lifetime predictions because HCD is known to be a strongly nonuniform phenomenon with substantially different concentrations N_{it} in different section of the device at the same stress time step. Instead, degradation of such parameters as the linear drain current and threshold voltage would be worthwhile to address. Furthermore, although the necessity of evaluating the carrier DF is acknowledged, in practice this information has not been incorporated in the approach.

To bridge the gap between the microscopic level of defect creation and the device modeling level, the Hess model was adapted for TCAD device simulations by Penzin et al. [57]. The model employs a phenomenological approximation and the microscopic level is not covered. As a result, the interplay between the SP and MP mechanisms is no longer addressed. The bond-rupture process is described by the kinetic equation for the passivated bond concentration. Similar to the original Hess model, the Penzin approach incorporates the dispersion of the activation energy of bond dissociation. Moreover, this activation energy is considered to be

dependent on the transversal component of the electric field and on the concentration of released hydrogen. According to the Penzin model, released hydrogen and remaining dangling bonds are charged. As a consequence, they strengthen the transversal electric field, which prevents the charged hydrogen ions from leaving the system, thereby effectively increasing the potential barrier that separates the bonded state and the transport mode.

The Penzin approach suffers from several shortcomings. For instance, it attempts to incorporate carrier transport into consideration. However, instead of evaluation of the carrier AI, the model is based on the "hot-carrier current." The definition of this quantity is vague because the criterion of how to separate cold and hot carriers is not provided in the paper. Moreover, cold carriers were shown also to contribute to the bond-breakage process by triggering the MVE process. Therefore, the AI seems to be more physically reasonable rather than the hot-carrier current. The consequence of this phenomenological simplification results also in a lack of information on the interface trap concentration N_{it}. Finally, although the model attempts to represent the characteristics of the degraded device, in practice we are not aware of such a comparison of the experimental data with simulation results.

3.2 Energy-Driven Paradigm

There are two main achievements associated with the energy-driven paradigm developed by Rauch and La Rosa; see [10, 25, 26, 38] and the corresponding chapter [27]. The first is the idea that in ultra-scaled MOSFETs, EES plays a dominant role (see [27], Sect. 6). Indeed, in scaled devices, hot electrons are rather unlikely, and if EES is not considered, the single-carrier mechanism is not probable. EES, however, populates the high-energy fraction of the particle ensemble and thus strengthens the SP process. Together with the MP mechanism, EES is responsible for HCD in short-channel MOSFETs and also determines the HCD temperature behavior in these devices in them.

Second, this approach claims that starting from the 180-nm node and beyond, the driving force of HCD is the energy deposited by carriers, not the electric field, [27], Sect. 4. The revolutionary aspect of this Rauch–La Rosa approach is that the fundamental driving force of HCD is changed. Pragmatically, the energy-driven paradigm allows to avoid computationally demanding calculations of the carrier DF and suggests a simplified treatment of carrier transport. This treatment is based on similarity of the impact ionization and bond-breakage rates. Indeed, both rates are described by expressions of the same functional form as the carrier AI [25–27], Sect. 5: $\int f(E)S(E)dE$ (cf. (1)), where $f(E)$ is the carrier energy DF, while $S(E)$ is the cross section of the corresponding reaction (see Fig. 11). The DF strongly decays with energy, while the reaction cross section shows a power law growth. The product $f(E)S(E)$, therefore, can have one or two maxima observed at certain energies. Due to the rapid decay of the integrand in the vicinity of these reference
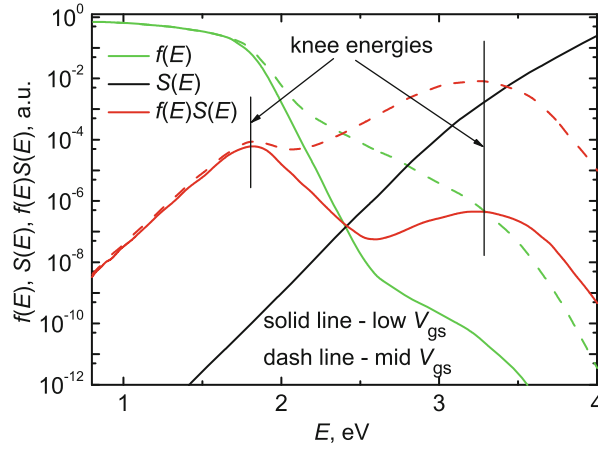
Fig. 11 A sketch of the energy-driven paradigm. Both the rate of impact ionization and the bond-breakage rate (for the SP mechanism) are determined by integrals of the same functional form as the AI: $\int f(E)S(E)dE$. The carrier DF $f(E)$ is a rapidly decaying function of energy, while the cross section $S(E)$ grows with energy as a power law. The product, therefore, results in a single maximum or two maxima pronounced at certain energies, and the main contribution to the rate is provided by these energies, known as "knee energies"

values, the rates of these processes are controlled by these energies. These energies are called "knee" and are weak functions of the applied drain voltage.

Therefore, the main message of the energy-driven paradigm is that one may avoid computationally expensive carrier transport treatment and use some empirical factors linked to stress/operating conditions instead of the carrier AI. Note also that the model parameters were adjusted based on the Monte Carlo simulations and in a manner to represent the degraded device characteristics. The main shortcoming of this paradigm is that it does not address the microscopic mechanisms of the defect creation and already operates at the device level. Therefore, the information on the interface state density N_{it} is not achievable and one of the main features of HCD—its strong localization—is not captured.

3.3 Bravaix Model

The model developed by Bravaix group captures some of the main physical ingredients of HCD, in particular the interplay between the SP and MP mechanisms and the idea that for proper description of these mechanisms, the carrier transport needs to be addressed [5, 24, 49], Sect. 3.A. However, the first version of the model was realized on the basis of the energy-driven paradigm. This was dictated by needs to make the Bravaix approach suitable for compact modeling and to directly link it with the lucky electron model. Thus, this version avoids calculations of the carrier

DF by means of the solution of the BTE and implements the bond-breakage rates being linked to the drain current via some empirical factors [5, 23]. Thus, the SP mechanism, EES, and the MP process are considered independent and related to three basic modes of HCD [23, 58].

Operating/stress voltages with high average carrier energies correspond to the HCD mode controlled by the SP process. This case is well described by the lucky electron model, and the device lifetime is evaluated as

$$1/\tau_{\mathrm{SP}} \sim (I_{\mathrm{d}}/W)(I_{\mathrm{sub}}/I_{\mathrm{d}})^m, \tag{6}$$

where $I_{\mathrm{d}}/I_{\mathrm{sub}}$ is the drain/substrate current, W is the device width, and the empirical factor $m \sim 2.7$ is the ratio between power factors in the reaction cross sections of the interface state generation process and impact ionization.

Another case corresponds to the high channel carrier flux with low carrier energies. These cold carriers are unlikely to trigger the SP mechanism, and therefore this mode is governed by the MP process. The device lifetime is

$$1/\tau_{\mathrm{MP}} \sim [(qV_{\mathrm{ds}}-\hbar\omega)^{1/2}(I_{\mathrm{sub}}/W)]^{E_{\mathrm{B}}/\hbar\omega}\exp(-E_{\mathrm{emi}}/k_{\mathrm{B}}T_{\mathrm{L}}) \approx [V_{\mathrm{ds}}^{1/2}(I_{\mathrm{d}}/W)]^{E_{\mathrm{B}}/\hbar\omega}. \tag{7}$$

To describe the MP process, one uses the truncated harmonic oscillator model for the Si–H bond [5, 49] and $\hbar\omega$ is the distance between the oscillator levels in the corresponding quantum well (see Fig. 10). The structure of this expression is discussed in more detail later.

An intermediate regime with moderate current densities and moderate carrier energies is governed by EES with the corresponding lifetime

$$1/\tau_{\mathrm{EES}} \sim (I_{\mathrm{d}}/W)^2(I_{\mathrm{sub}}/I_{\mathrm{d}})^m. \tag{8}$$

This quadratic signature results from impact ionization, which generates electron–hole pairs that are still cold in terms of bond breakage. However, these carriers can be further converted by EES into high-energy particles, thereby contributing to the single-carrier bond-breakage process.

Under stress/operating conditions, these three processes (considered independent) lead to the device lifetime, which is a superposition of lifetimes of each particular HCD mode:

$$1/\tau_{\mathrm{d}} = K_{\mathrm{SP}}/\tau_{\mathrm{SP}} + K_{\mathrm{EES}}/\tau_{\mathrm{EES}} + K_{\mathrm{MP}}/\tau_{\mathrm{MP}}. \tag{9}$$

In other words, different contributions are weighted with empirical prefactors that reflect probabilities of each particular process, that is, the competing nature of EES, SP and MP mechanisms.

Within the Bravaix model, the MP process is described using the truncated harmonic oscillator model of the Si–H bond [24, Sect. 3.C]. Following the approach

developed by the Hess group, Bravaix et al. solve the system of rate equations, which describes the kinetics of the oscillator [5]:

$$\frac{dn_0}{dt} = P_d n_1 - P_u n_0$$
$$\frac{dn_i}{dt} = P_d(n_{i+1} - n_i) - P_u(n_i - n_{i-1}) \tag{10}$$
$$\frac{dn_{N_l}}{dt} = P_u n_{N_l-1} - R_{MP} N_{it}[H^*].$$

Here the system is written in a simplified manner. For instance, a term representing passivation of the dangling bonds is omitted in the equation for the last bonded state labeled as N_l. In this system, P_u/P_d designate the bond excitation/deexcitation rates, R_{MP} stands for bond breakage from the last bonded state, while $[H^*]$ represents the concentration of released hydrogen. Note that a bond-breakage rate is included only in the last equation. This means that only bond dissociation from the last bonded state is considered, as opposed to the Hess model, where contributions of all levels are respected [7]. Also, bond rupture from the ground level was not incorporated in the system (10) because this corresponds to the SP process, which was considered an independent mechanism [5, 28, 49]. The rates P_u and P_d are

$$P_u = \int I_d \sigma \, dE_e + \omega_e \exp(-\hbar\omega/k_B T_L) = S_{MP}(I_e/e) + \omega_e \exp(-\hbar\omega/k_B T_L)$$

$$P_d = \int I_d \sigma \, dE_e + \omega_e = S_{MP}(I_e/e) + \omega_e. \tag{11}$$

Here the carrier AI $\int I_d \sigma \, dE_e$ is treated in terms of the energy-driven paradigm and thus is substituted by the drain current I_d weighted with the empirical factor S_{MP}.

The solution of the rate equation system (11) leads to the cumulative rate for the MP process [5, 15]:

$$R_{MP} \sim N_0 \left[\frac{S_{MP}(I_d/e) + \omega_e \exp(-\hbar\omega/k_B T_L)}{S_{MP}(I_d/e) + \omega_e} \right]^{E_B/\hbar\omega} \exp(-E_{emi}/k_B T_L). \tag{12}$$

The simplified solution of the system (10) for the case of a low bond-breakage rate $R_{MP}t \ll 1$ is

$$N_{it} = (N_0 R_{MP} [P_u/P_d]^{E_B/\hbar\omega}) t^{1/2}. \tag{13}$$

The factor $E_B/\hbar\omega$ represents the number of levels in the oscillator potential well and also enters the formula (7), which describes the device lifetime for the MP-driven mode.

In the recent version of the Bravaix model, the authors have developed an extended formalism that accounts for the progressive change of the degradation regime from the EES mode to the bond dissociation controlled by the MP

Fig. 12 The interface state density as a function of the lateral coordinate $N_{\mathrm{it}}(x)$: experimental data extracted from the charge-pumping measurements (*dashed lines*) vs. simulated by the Bravaix model $N_{\mathrm{it}}(x)$ profiles (*solid lines*). One can see that the $N_{\mathrm{it}}(x)$ maximum is located near the drain end of the gate. A good agreement is achieved between experiment and theory
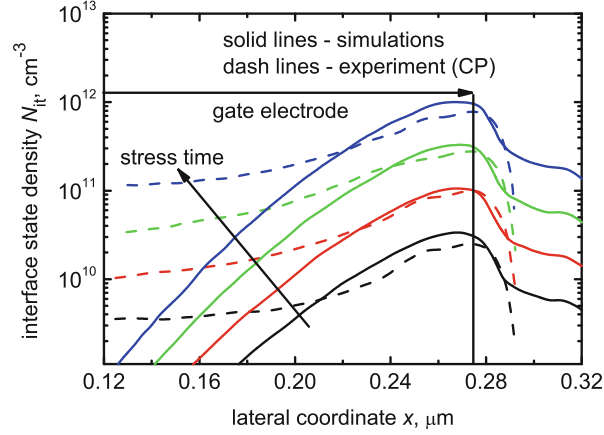
mechanism [19, 24], Sect. 4.A. In this case, the bond-breakage rate is described by a more complex expression:

$$S_{\mathrm{SP}}(E) = 0, \qquad\qquad E < 1.5\,\mathrm{eV}, \tag{14}$$

$$S_{\mathrm{SP}}(E) = \mathrm{const}, \qquad\qquad 1.5 \le E < 1.9\,\mathrm{eV}, \tag{15}$$

$$S_{\mathrm{SP}}(E) = \alpha \exp(3E), \qquad 1.9 \le E < 2.5\,\mathrm{eV}, \tag{16}$$

$$S_{\mathrm{SP}}(E) = \beta(E - 1.5)^{11}, \qquad E \ge 2.5\,\mathrm{eV}. \tag{17}$$

This formula includes all three regimes and is still based on the knee energy concept. Such a treatment does not require computationally demanding evaluations of the carrier distribution function; however, it introduces some additional fitting parameters. Finally, this strategy allows the authors to properly represent not only the change with time of such device characteristics as the threshold voltage and transconductance, but also the interface trap density extracted from the charge-pumping data [18, 28] (see Fig. 12).

One of the newest developments within the Bravaix model suggests that the role of EES in the context of HCD is dramatically overestimated see [19] and the corresponding chapter [24], Sect. 4.A. To address the role of EES, the authors used ultra-scaled MOSFETs with a gate length of 30 nm. The devices were subjected to hot-carrier stress at various combinations of V_{ds} and V_{gs} striving to cover both regimes governed by SP and MP mechanisms. It was demonstrated that although EES can substantially change the shape of the carrier energy distribution function, this population of the high-energy tail of the DF does not really translate into enhancement of hot-carrier damage at all stress conditions studied [19]. Instead, the authors suggest that the damage is dominated by the mixed-mode regime, that is, by the progressive change from EES to the MP mechanism.

Note finally that the model is capable of covering the temperature behavior of HCD; see [24], Sect. 3.B, and [49, 59]. For instance, this behavior appears to

change when device dimensions shrink to the nanometer range. In this range, the MP process is usually dominant and the HCD temperature behavior is controlled by (12), which contains the temperature-dependent drain current and the Arrhenius-type term describing hydrogen release from the last bonded state to the transport mode. If the effect of the former contribution is stronger than the latter one, this leads to a simplified formula (7) [49]. Moreover, new improvements have been brought to the Bravaix modeling approach recently, as detailed in this book; see [24].

Although the model can capture main features of HCD and does not rely on time-consuming simulations of the carrier distribution functions, it suffers from some shortcomings. First of all, the model considers SP and MP mechanisms and EES as independent processes. Such a treatment is not physically reasonable because bond breakage leads to interface traps, which can capture charge carriers, become charged, and thereby distort the distribution function and hence the rates of the scattering mechanisms. However, these scattering mechanisms impact the DFs and, as a consequence, the rates of the SP and MP processes. Therefore, all of these processes need to be considered self-consistently. The authors suggest that EES does not play a significant role relevant to HCD in scaled devices. At the same time, there is some evidence that EES is crucial for ultra-scaled devices and changes the HCD temperature behavior in them.

4 Our Model Based on the Exact Solution of the Boltzmann Transport Equation

We already discussed that for proper understanding and modeling of HCD, one must cover and link all the levels related to this detrimental phenomenon. The energy exchange mechanisms affect the shape of the carrier DF, which determines the rates of the bond-breakage mechanisms. Therefore, careful treatment of the carrier transport needs to be the kernel of a physics-based HCD model. As an adjustment problem, the microscopic level of defect generation also needs to be incorporated in the simulation framework and linked to the transport module. Finally, the model has to properly describe degradation of the MOSFET characteristics during hot-carrier stress, and thus the simulation of the degraded devices is another essential subtask.

4.1 The HCD Model Based on the Stochastic Boltzmann Transport Equation Solver

The first version of our physics-based HCD model [17, 60–62] was realized on the basis of a stochastic Boltzmann transport equation solver MONJU, which uses the Monte Carlo method [21]. The model structure is presented in [8, 61]. MONJU was employed to calculate the carrier energy DFs in each point at the interface for
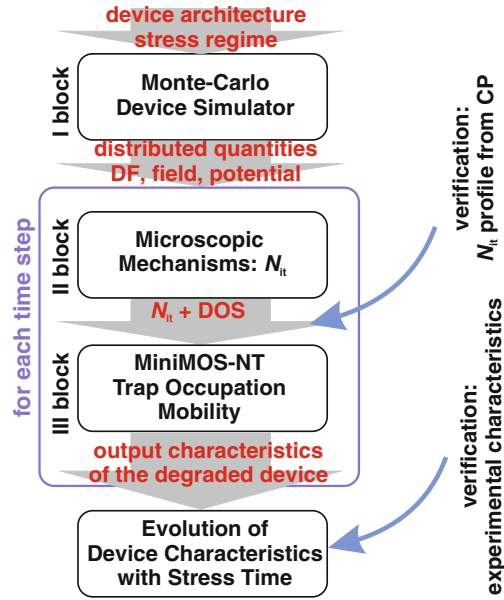
Fig. 13 The structure of our physics-based HCD model. The model includes three main subtasks: the carrier transport kernel; a module that describes microscopic mechanisms of defect generation; and the module needed for modeling of the degraded devices. As the carrier transport kernel, a stochastic BTE solver MONJU is used. MONJU calculates the carrier DF at the interface for the particular device geometry and stress conditions. These DFs are then used as the input data for the module, which calculates the interface state density as a function of the lateral coordinate and stress time $N_{it}(x, t)$. This $N_{it}(x, t)$ is then loaded into the device simulator MiniMOS-NT, which calculates the characteristics of the degraded device at each stress time step

the particular device architecture and given stress/operating conditions. MONJU incorporates such energy exchange mechanisms as scattering at ionized impurities, surface scattering, impact ionization, and electron–phonon scattering. Note that EES is not implemented in MONJU, and therefore this simulator is not applicable for ultra-scaled devices where EES plays an important role.

The information about the carrier DF is then used as input data for the module, which describes the bond-breakage kinetics. The output of this module is the interface state density as a function of the lateral coordinate. These $N_{it}(x)$ profiles are calculated for each stress time step, and therefore the $N_{it}(x, t)$ table is generated and then used to simulate the device characteristics of the degraded MOSFETs. For this purpose, the device simulator MiniMOS-NT is employed, which is based on simplified approaches to the BTE solution, namely, on drift diffusion (DD) and energy transport (ET) schemes [63]. This also limits the applicability of the model because the DD and ET models are applicable only for MOSFETs with channel lengths not shorter than $\sim$0.1 μm. In this version of the model, all these subtasks have been solved subsequently using different device simulators for each particular

task. Distribution functions were evaluated only once, that is, were not refined at each stress time step according to generated charged defects. This was related to the stochastic nature of the time-consuming Monte Carlo method. Using MONJU also for simulations of the characteristics of the degraded devices would make the model calibration process not achievable within a reasonable time slot.

The key quantity in our model that controls HCD is the carrier AI. The AI is calculated using the carrier DF obtained from MONJU for both SP and MP mechanisms and for electrons and holes:

$$I_{SP/MP}^{(e/h)} = \int_{E_{th}}^{\infty} f^{(e/h)}(E)g^{(e/h)}(E)\sigma_{SP/MP}^{(e/h)}(E)v(E)dE, \tag{18}$$

where $f^{(e/h)}(E)$ is the carrier DF for electrons/holes, $g^{(e/h)}(E)$ is the density of states, $v(E)$ is the group velocity, while $\nu_{SP/MP}^{(e/h)}$ is a prefactor that represents the attempt frequency, $\sigma_{SP/MP}^{(e/h)}$ is the Keldysh-like reaction cross section for the SP and MP mechanisms triggered by electrons or holes [61]:

$$\sigma_{SP/MP}^{(e/h)}(E) = \sigma_{0,SP/MP}^{(e/h)}(E - E_{th,SP/MP})^{p_{it}}, \tag{19}$$

with $\sigma_{0,SP/MP}$ being the attempt rate and $p_{it} = 11$. The threshold energy is $E_{th} = 1.5\,\text{eV}$ for both processes.

Within this version of the model, we considered the SP and MP mechanisms independent. For the former one, the bond-breakage rate was equal to the carrier AI weighted with an attempt frequency $\nu_{SP/MP}^{(e/h)}$:

$$R_{SP}^{(e/h)} = \nu_{SP}^{(e/h)} I_{SP}^{(e/h)}. \tag{20}$$

If we assume the first-order kinetics for this mechanism, the corresponding portion of the interface state density is found to be

$$N_{SP}(t) = N_0 \left[1 - e^{-(\nu_{SP}^{(e)} I_{SP}^{(e)} + \nu_{SP}^{(h)} I_{SP}^{(h)})t} \right], \tag{21}$$

where N_0 is the concentration of "virgin" bonds available for dissociation.

The kinetics of the MP process has been described within the truncated harmonic oscillator model (see Fig. 10). Mathematically, the density of interface states generated by this process can be found as a solution of the rate equation system:

$$\begin{aligned}
\frac{dn_0}{dt} &= P_d n_1 - P_u n_0 \\
\frac{dn_i}{dt} &= P_d(n_{i+1} - n_i) - P_u(n_i - n_{i-1}) \\
\frac{dn_{N_l}}{dt} &= P_u n_{N_l-1} - P_d n_{N_l} - R_{MP} n_{N_l} + \tilde{P}_{MP} N_{MP}^2,
\end{aligned} \tag{22}$$

which is modified compared to that used in the Bravaix model [5]—cf. (10)—in a manner to incorporate the dangling-bond passivation process as well. To satisfy the dimensionality, here we use $\tilde{P}_{\text{MP}} = P_{\text{MP}}/N_0$. The dissociation/passivation rates are defined following the Arrhenius relation:

$$
\begin{aligned}
R_{\text{MP}} &= \nu_{\text{MP,act}} \exp\left(-E_{\text{emi}}/k_{\text{B}}T_{\text{L}}\right), \\
P_{\text{MP}} &= \nu_{\text{MP,pass}} \exp\left(-E_{\text{pass}}/k_{\text{B}}T_{\text{L}}\right),
\end{aligned}
\tag{23}
$$

where E_{emi}, E_{pass} are barriers for hydrogen hopping from the last bonded state to the transport mode and back, respectively (see Fig. 10). Prefactors $\nu_{\text{MP,act}}$ and $\nu_{\text{MP,pass}}$ are the attempt rates.

We solve this system by using the timescale hierarchy, which is due to the huge disparity between the time constants describing the oscillator steady-state establishment and those of the much slower bond-breakage/passivation processes, which are related to hydrogen hopping between the last bonded state N_{l} and the transport mode. In other words, we omit two last terms in the equation for the N_{l} level and solve the system recurrently, thereby finding the occupancy of levels. This results in the following interrelations between occupation numbers: $n_i/n_0 = (P_{\text{u}}/P_{\text{d}})^i$ (note that for the sake of simplicity, we consider that the bond is predominantly situated in the ground state, i.e., $N_0 = \sum n_i \approx n_0$).

Then the passivation/depassivation rates are returned back to the system (22) and we assume that occupation numbers n_i do not change during slow dissociation/passivation processes. The solution obtained with the boundary condition that initially all the bonds are virgin is

$$
N_{\text{MP}} = N_0 \left(\frac{R_{\text{MP}}}{P_{\text{MP}}} \left(\frac{P_{\text{u}}}{P_{\text{d}}} \right)^{N_{\text{l}}} \left(1 - e^{R_{\text{MP}}t}\right) \right)^{1/2}.
\tag{24}
$$

Note that for weak stresses and/or short stress times, meaning $R_{\text{MP}}t \ll 1$, a Taylor expansion gives the approximation $1 - \exp(-R_{\text{MP}}t) \approx R_{\text{MP}}t$, and one obtains the square-root time dependence, as in the Bravaix model [5, 49].

The rates P_{u} and P_{d} for excitation and decay of the Si–H bond vibrational modes are defined similarly to expressions (11) used in the Hess and Bravaix models:

$$
\begin{aligned}
P_{\text{u}} &= \nu_{\text{MP}}^{(e)} I_{\text{MP}}^{(e)} + \nu_{\text{MP}}^{(h)} I_{\text{MP}}^{(h)} + \omega_{\text{e}} \exp\left(-\hbar\omega/k_{\text{B}}T_{\text{L}}\right), \\
P_{\text{d}} &= \nu_{\text{MP}}^{(e)} I_{\text{MP}}^{(e)} + \nu_{\text{MP}}^{(h)} I_{\text{MP}}^{(h)} + \omega_{\text{e}}.
\end{aligned}
\tag{25}
$$

While considering the total concentration of the interface states, one should take into account the competing nature of SP and MP modes and weight their contributions with certain probabilities:

$$
N_{\text{it}} = p_{\text{SP}} N_{\text{SP}} + p_{\text{MP}} N_{\text{MP}}.
\tag{26}
$$
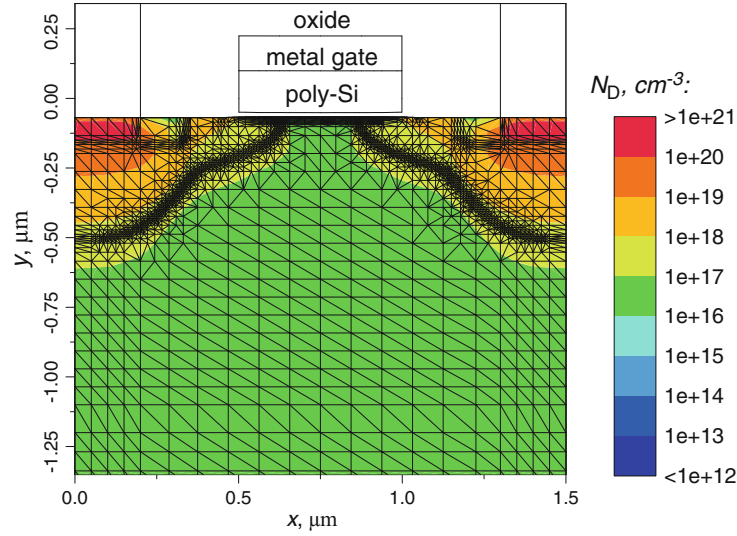
Fig. 14 The architecture of the 5V n-MOSFET with the 0.5 μm channel length used for model validation. The phosphorous doping profile is represented by the *color map*

Note that dependence on the lateral coordinate enters the resulting concentration via the carrier AI based on the carrier DF, which can be substantially different in different sections of the MOSFET.

The model has been calibrated in a manner to represent the change ΔI_{dlin} vs. stress time of the linear drain current (i.e., the current measured at $V_{ds} = 0.1$ and $V_{gs} = 5.0$ V) observed in 5V n-MOSFETs [we use the relative change, i.e., normalized with respect to the current in the fresh device: $\Delta I_{dlin}(t) = (I_{dlin}(t) - I_{dlin0})/I_{dlin0}$]. The main demand on the model was that the model must represent experimental $\Delta I_{dlin}(t)$ measured in different devices but using the same set of the model parameters [61]. For this purpose, we used a series of 5V n-MOSFETs of an identical architecture but with different channel lengths of 0.5, 1.2, and 2.0 μm. The sketch of the 0.5 μm device is presented in Fig. 14.

A family of typical electron distribution functions calculated for the 0.5 μm transistor evaluated for $V_{gs} = 2.0$ V and $V_{ds} = 6.25, 6.75, 7.25$ V and room temperature is plotted in Fig. 15. One can see that the DFs calculated near the drain and source are close to the Maxwellian distribution. This behavior is reasonable because the source and drain act as reservoirs of cold carriers that are in equilibrium. If we move closer to the device center, the carrier DFs appear to become severely nonuniform, demonstrating long high-energy tails; however, a Maxwellian rudiment is still pronounced at low energies (green curves). These rudiments are not visible in DFs calculated for the drain end of the gate, exactly in the place where the carrier AI computed using these DFs has a peak. Instead, the high-energy tails are best pronounced, and also a plateau is visible at moderate energies. Note that these high-energy tails become longer if the drain voltage V_{ds} increases. The family of
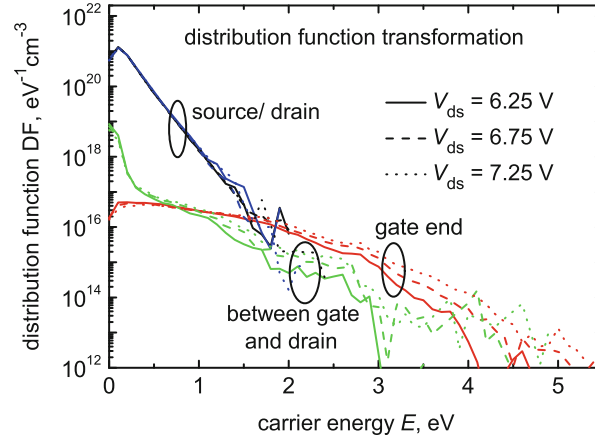
**Fig. 15** The carrier distribution functions calculated for the 5V n-MOSFET with a 0.5 μm channel length for $V_{gs} = 2.0$ V and $V_{ds} = 6.25$, 6.75, and 7.25 V. Particular DFs at the source, in the center of the channel, beyond the drain end of the gate, and at the drain are plotted. Source and drain DFs are close to the Maxwellian distribution, but others are severely non-equilibrium. The DF computed at the drain end of the gate corresponds to the peak of the carrier AI (see Fig. 16) and has long high-energy tails
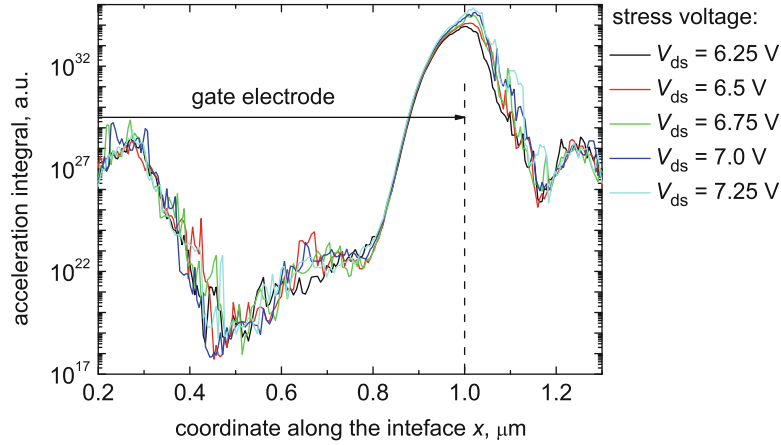
Fig. 16 The carrier AI calculated for the 5V n-MOSFET with a 0.5 μm channel length for $V_{gs} = 2.0$ V and $V_{ds} = 6.25$, 6.5, 6.75, 7.0, and 7.25 V. One can see that the AI peak is situated near the drain end of the gate, which reflects the localized nature of HCD

the corresponding carrier AIs calculated for a fixed $V_{gs} = 2.0$ V and a series of $V_{ds} = 6.25$, 6.5, 6.75, 7.0, and 7.25 V is shown in Fig. 16. One can see that for all values of V_{ds}, the AI features a maximum near the drain end of the gate. This behavior reflects the localized nature of the HCD phenomenon. In general, values of the AI become higher as V_{ds} increases.
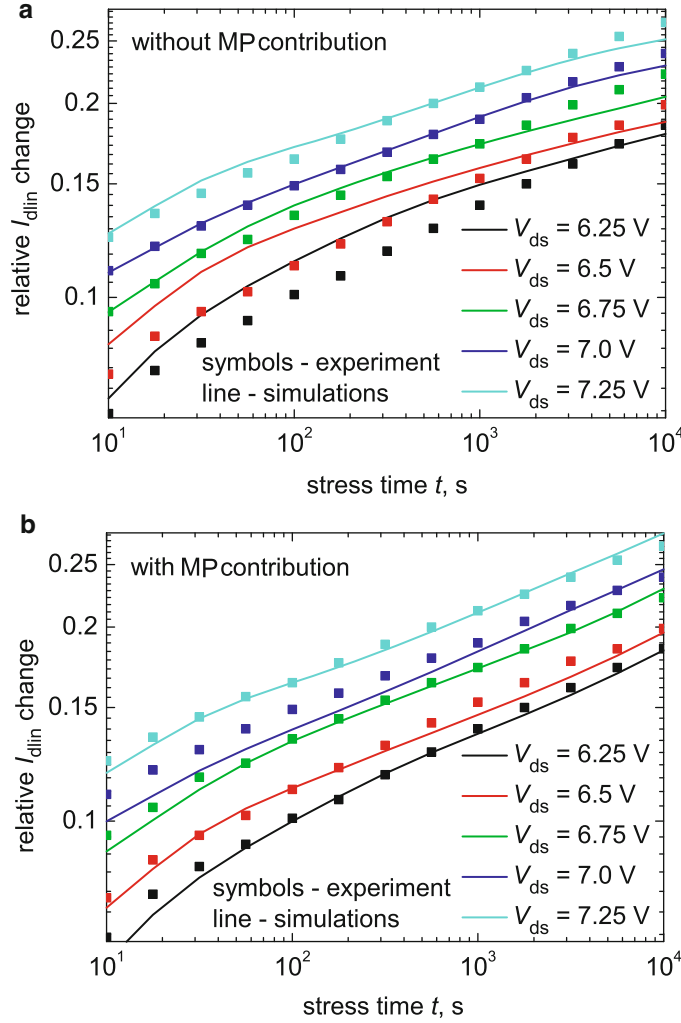
Fig. 17 The linear drain current change ΔI_{dlin} as a function of time plotted for different stress conditions ($V_{\mathrm{gs}} = 2.0\,\mathrm{V}$ and $V_{\mathrm{ds}} = 6.25, 6.5, 6.75, 7.0,$ and $7.25\,\mathrm{V}$): experiment vs. simulations. To demonstrate importance of the MP mechanism even in long-channel devices, the ΔI_{dlin} curves are calculated ignoring the MP-process contribution (**a**). This leads to spurious results. The $\Delta I_{\mathrm{dlin}}(t)$ curves simulated when considering the MP process properly represent the experimental data (**b**)

The earliest version of our model considered only the contribution of the minority carriers (electrons in the case of n-MOSFETs) and was calibrated to represent $\Delta I_{\mathrm{dlin}}(t)$ curves measured in the $0.5\,\mu\mathrm{m}$ n-MOSFETs [17, 60] (from the family discussed above) stressed at a fixed $V_{\mathrm{gs}} = 2.0\,\mathrm{V}$ and a series of $V_{\mathrm{gs}} = 6.25,$ 6.5, 6.75, 7.0, and $7.25\,\mathrm{V}$ at room temperature for $10^4\,\mathrm{s}$. For instance, Fig. 17 demonstrates a quite good agreement between experimental and simulated $\Delta I_{\mathrm{dlin}}(t)$

characteristics. Figure 17b shows that if the MP process is ignored, the simulated curves of the linear drain current change vs. time are spurious. Therefore, it is important to emphasize that the MP process still plays a considerable role even in the case of long-channel MOSFETs stressed at $V_{ds} = 6.25$ V and higher.

Figure 18 summarizes the interface state density profiles calculated for the $V_{gs} = 2.0$ V and $V_{ds} = 6.25$ V for the whole range of stress time (a) as well as the relative contribution of the MP process into N_{it} (b). The N_{it} peak is situated near the drain end of the gate and corresponds to the AI maximum; cf. Fig. 16. The carriers in this device section are rather hot, thereby efficiently triggering the SP mechanism. In the drain area and in the MOSFET center, carriers are colder, and thus HCD is dominated by the MP process, which leads to ledges surrounding the N_{it} maximum.
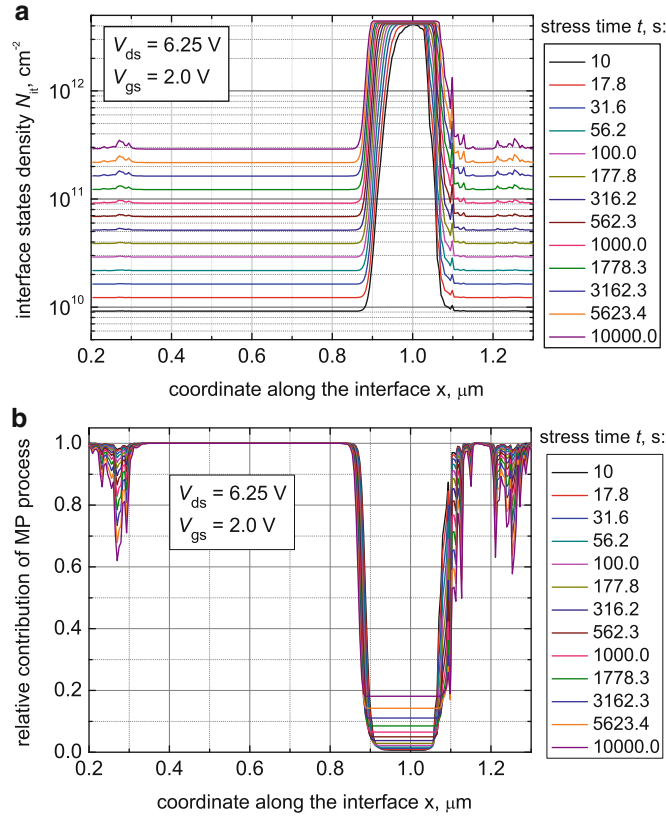
Fig. 18 The interface state density profiles $N_{it}(x)$ (**a**) plotted for each stress time and for stress conditions $V_{gs} = 2.0$ V, $V_{ds} = 6.25$ V and the relative contribution of the MP process (**b**). One can see that the SP process is responsible for the N_{it} peak, while the MP mechanism controls HCD in the center of the device and close to the drain. The latter mechanism is saturated (due to high stress voltages) and thus leads to coordinate independent interface state density (ledges surrounding the N_{it} maximum)

Fig. 19 The linear current degradation measured at $V_{gs} = 2.0\,V$ and $V_{ds} = 6.25\,V$ in three devices (with $L_{ch} = 0.5$, 1.2, and $2.0\,\mu m$) plotted against the curves simulated with the model calibrated for the $0.5\,\mu m$ MOSFET. The model completely fails to represent HCD in longer devices
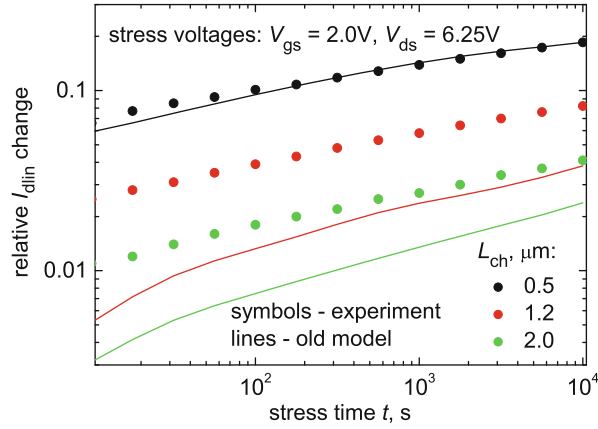

This is because at these high voltages, the MP mechanism is saturated and leads to a coordinate-independent contribution. Such a finding correlates well with results later presented by the Bravaix group [18].

Despite the success in modeling of the drain current change in a particular device, the model version that considers only electrons failed to represent $\Delta I_{dlin}(t)$ curves measured in the family of three devices. Figure 19 summarized the $I_{dlin}(t)$ data obtained in devices with the channel lengths of $L_{ch} = 0.5$, 1.2, and $2.0\,\mu m$ at $V_{gs} = 2.0\,V$ and $V_{ds} = 6.25\,V$ as well as $\Delta I_{dlin}(t)$ curves obtained with the model calibrated in order to represent HCD in the $0.5\,\mu m$ device. One can see that the model dramatically underestimates HCD in longer devices. To understand this behavior, we plotted the average interface trap concentration $\langle N_{it} \rangle$ [i.e., $N_{it}(x)$ integrated over the interface and then divided by the interface length] for all three devices as a function of time (see Fig. 20). One can see that the shortest device demonstrates the lowest value of $\langle N_{it} \rangle$ in the entire stress time slot. The linear drain current change $\Delta I_{dlin}(t)$, however, is the highest among those measured in three devices under test.

This is because the concentration of interface traps generated by channel electrons peaks outside the MOSFET channel, that is, already between the gate and the drain (see Fig. 18). The device is less sensitive to traps located in the drain area compared to those situated in the channel. Therefore, the device performance is weakly affected by electron-induced interface states. A comparison of Figs. 19 and 20 suggests that the longer devices are less sensitive to the electron-induced N_{it} and that another mechanism leading to N_{it} created closer to the channel has to be responsible for this discrepancy. This missing contribution can be related to the secondarily generated (by impact ionization) holes. Impact ionization creates electron–hole pairs, and the carriers created by this process are then separated by the electric field (Fig. 21). The field accelerates holes toward the source. At the same time, holes need some distance to gain enough energy from the electric field to
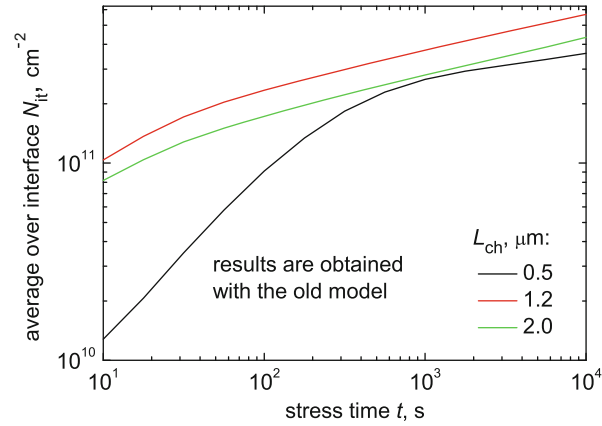
Fig. 20 The average interface state density $\langle N_{it} \rangle$ (i.e., the interface state density integrated over the interface and then divided by the interface length) plotted for three devices vs. stress time. One can see that the shortest device is characterized by the lowest values of $\langle N_{it} \rangle$ in the whole experimental time window. One may envisage that ΔI_{dlin} will also be highest in this device. However, Fig. 19 shows the opposite trend
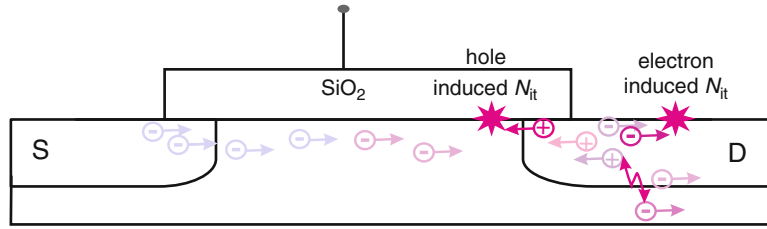
Fig. 21 The secondary holes generated by impact ionization are separated from electrons by the electric field and then accelerated toward the source. They need some distance to pass before they gain energy, which is enough to trigger the SP mechanism or to contribute to the MP process

trigger an SP mechanism or significantly contribute to the MP process. As a result, the hole-related portion of interface traps is expected to be shifted toward the source, as compared to the electron-induced one.

By considering the contribution made by holes, the model was calibrated in order to represent the $\Delta I_{dlin}(t)$ curves for all three devices and using the same set of model parameters [61]. The AIs plotted together with N_{it} profiles are presented in Fig. 22. In all devices, the peak of the hole AI is shifted toward the source respectively it is shifted from the electron maximum. The distance between these peaks increases with the device channel length. This means that long-channel transistors are more sensitive to the hole-induced traps than their shorter counterparts, and hence less sensitive to the traps induced by channel electrons, as expected. The interface state density also demonstrates maxima that coincide with the peaks of electron and hole
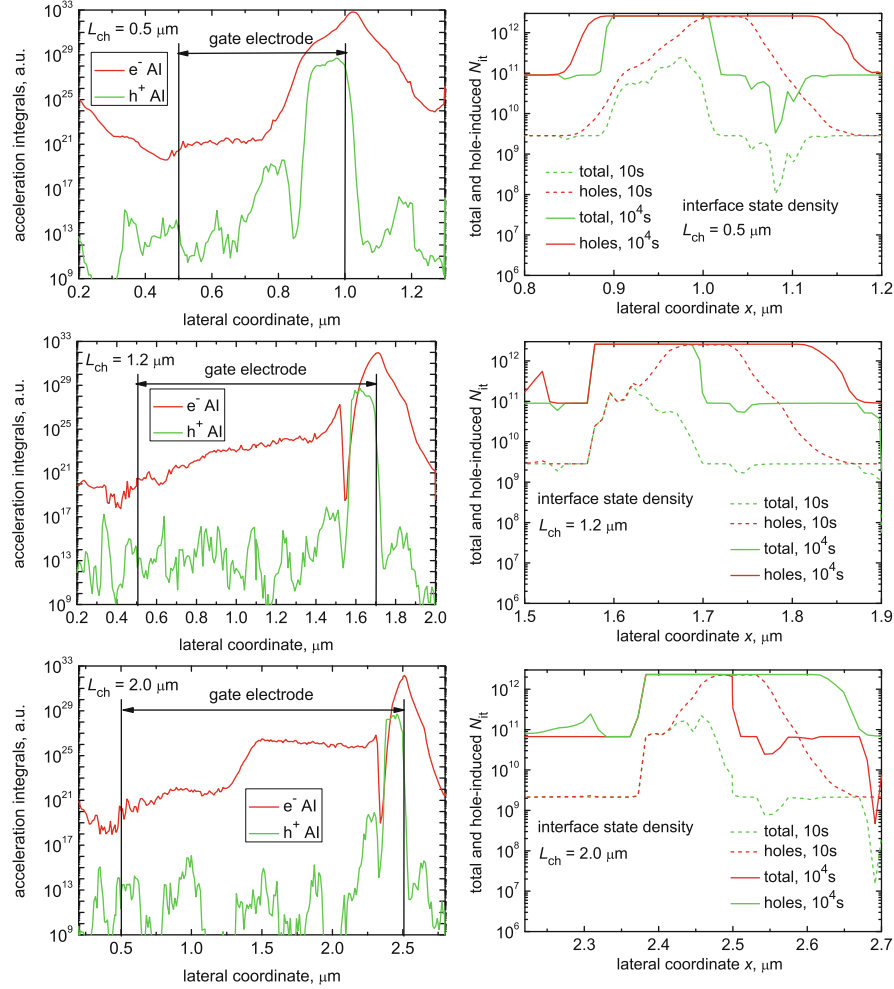
Fig. 22 The electron and hole AIs plotted vs. the lateral coordinate x as well as interface state density profiles $N_{it}(x)$ simulated considering contributions of both electrons and holes and only holes for stress times of 10 and 10^5 s. The hole AI peak is shifted toward the source compared to the electron-induced one. As a consequence, the density N_{it} calculated considering the hole contribution becomes wider and at long stress times (10^5 s) features a plateau, which appears when electron- and hole-related peaks interlock

AI (see [36, 64]). Note that in the newest version of the model, the N_{it} peak becomes substantially wider compared to the peak simulated with the model that ignores the hole contribution (cf. Fig. 18).

Finally, the model was calibrated in a way to represent HCD in these three devices using the same set of model parameters. Figure 23 demonstrates a good agreement between experimental and theoretical ΔI_{dlin} time dependencies. For comparison, we also plotted $\Delta I_{dlin}(t)$ curves simulated considering only the electron
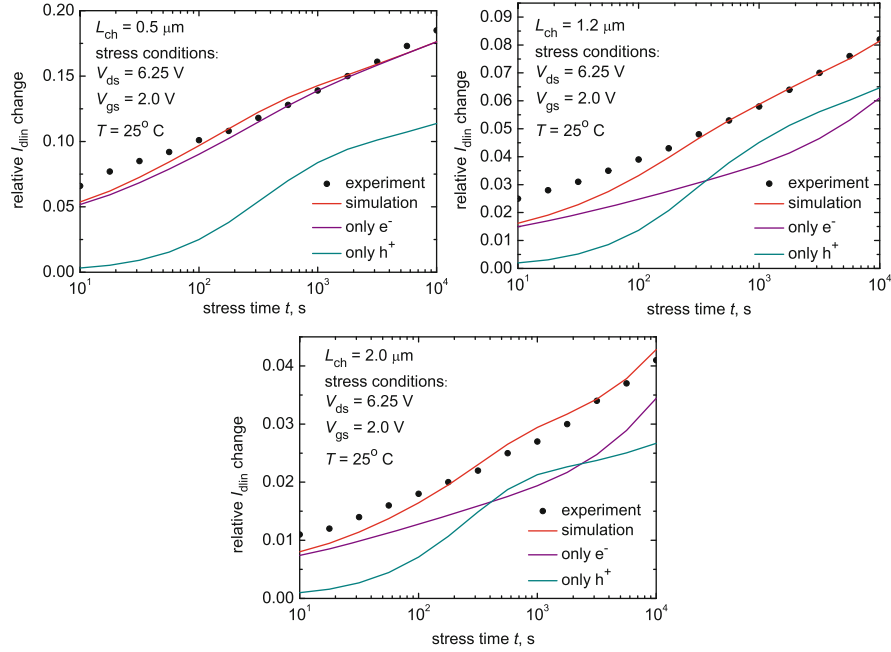
Fig. 23 The experimental $\Delta I_{\mathrm{dlin}}(t)$ data plotted against simulated ones for the n-MOSFETs with channel lengths of 0.5, 1.2, and 2.0 μm. For comparison, a linear drain current degradation simulated considering only the electron and hole contribution is also depicted. This comparison shows that both types of carriers need to be incorporated in the model

or hole contribution in HCD. One can see the importance of the hole-related damage increases in the case of long-channel devices. This correlates with the idea that long-channel MOSFETs are less sensitive to the electron-induced portion of damage. Note that in the case of the 0.5 μm device, HCD can be represented taking into account only the degradation portion produced exclusively by channel electrons.

Our HCD model is rather complex, and the model component that demands substantial computational resources is the carrier transport module. Therefore, the possibility of using simplified (and more computationally efficient) approaches that allow us to substitute the Monte Carlo method of carrier transport treatment appears to be very attractive. Among these approaches are DD and ET schemes for solving the BTE [65]. The question of whether these simplified approaches can adequately capture hot-carrier effects in scaled devices (with the channel length less than 0.1 μm) has already repeatedly arisen in the literature (see [66, 67] and the references therein). For instance, a thorough analysis of the DD and ET scheme applicability was performed in [66], and the results of these methods were compared with the exact BTE solution using the MC approach. This analysis has demonstrated that DD and ET methods can be applicable to describe transport in MOSFETs with channel lengths not shorter than 0.1 μm. At the same time, our physics-based HCD

model was calibrated in a manner to represent the degraded device characteristics employing MOSFETs with a channel length of $0.5\,\mu$m and longer. Therefore, one may envisage that DD and ET schemes can be applicable also for HCD modeling in these long-channel devices. These transistors were stressed at high V_{ds}, and HCD is dominated by the SP process. This mechanism is controlled by the high-energy tails of the carrier DF, and the model results are expected to be very sensitive to the particular transport scheme used for evaluation of the DF.

To check the applicability of ET and DD schemes, we compared the results of three versions of our HCD model, namely, that based on the exact BTE solution using the Monte Carlo method, the version based on the ET simulations, and the model where the DF is evaluated employing the DD scheme. In the ET-based version, only the average energy is taken from the Monte Carlo solution in order to emulate the solution of an ET model. The carrier DF is then evaluated in each position at the interface using the average carrier energy $\langle E \rangle(x)$ obtained from the ET scheme. This procedure is widely used in the ET-based physical models (see, e.g., [68]), and the DF is found to be $f(E) = A \exp[-E/\langle E \rangle]$, with A being a normalization constant. In the DD-based model, only the electric field lateral profile calculated with the Monte Carlo approach is retained. This field profile is then converted into the average carrier energy as [65]: $\langle E \rangle = 3k_B T_L/2 + q\tau_E \mu F^2$, where q is the electron charge modulus, τ_E the energy relaxation time, μ the carrier mobility, and F the electric field. Note that in order to eliminate a possible origin of discrepancy related to different device simulators, we performed all the calculations within MONJU.

Figure 24 summarizes the electron AIs (for the hole AIs, all tendencies are comparable) and interface density profiles calculated with MC-, ET-, and DD-based versions of our HCD model. In the DD-based version, the driving force of HCD is the electric field. However, it is well known that the carrier average energy and the DF follow the electric field with a certain delay [69]. This trend explains why the AI maximum (and hence, the $N_{it}(x)$ peak) appears shifted toward the drain compared to the $F(x)$ peak in the case of the DD-based model. We already discussed (see Fig. 5) that starting from the source to the drain, first the maximum of the electric field appears, followed by the carrier average energy, and finally by the position where the carrier DF demonstrates the most prolonged high-energy tails (calculated with the Monte Carlo method). Since different versions of our model are based on these quantities, the peaks of the electron AI appear in the same order (see Fig. 24).

This tendency is also confirmed by the maxima of $N_{it}(x)$ profiles calculated using different transport schemes. Another characteristic feature is that the interface trap density computed with the ET-based model spuriously overestimates the damage compared to DD- and MC-based models. Such a trend was expected based on our hot-carrier tunneling studies [68], where the tunneling process rate was also overestimated when the DF was simulated employing the ET scheme. The linear drain current change (see Fig. 25) also follows this trend, and thus the I_{dlin} degradation is dramatically overestimated when being calculated with the ET-based approach and also much stronger than those predicted if DD and MC schemes are used. Finally, the DD-based model predicts ΔI_{dlin} close to the result obtained by
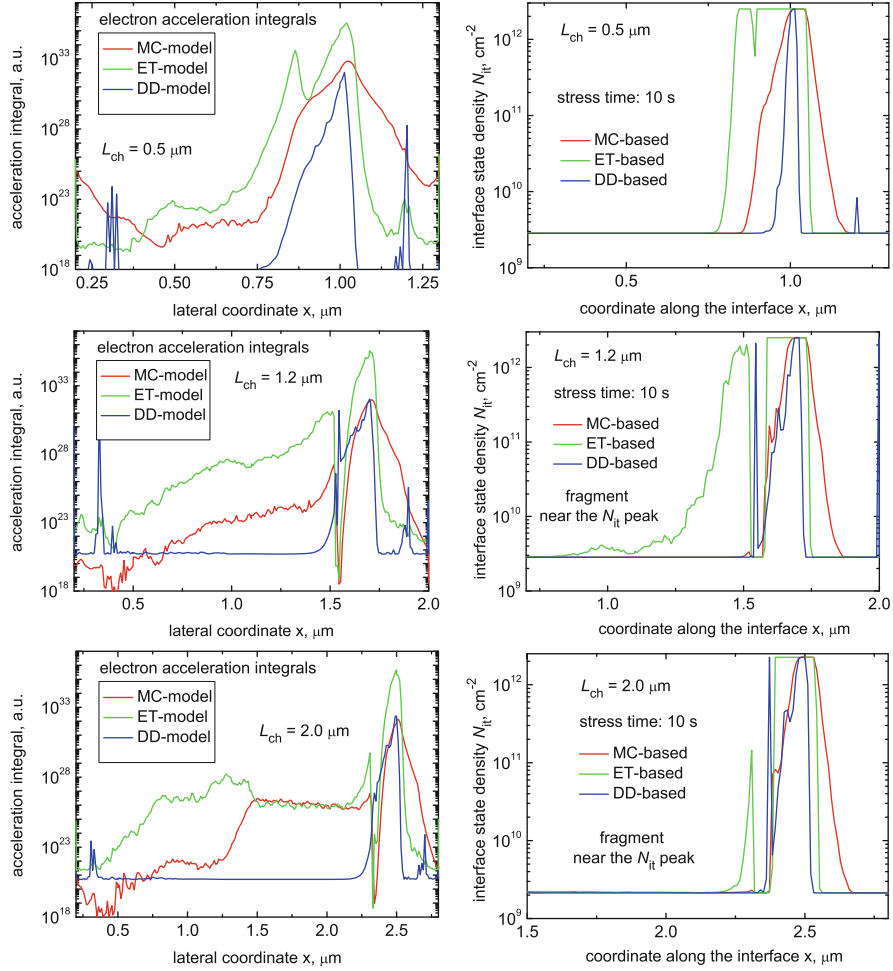
Fig. 24 The electron AI and interface state density profiles $N_{it}(x)$ calculated using the MC-, ET-, and DD-based versions of our HCD model for 0.5-, 1.2-, and 2.0 μm devices and for a stress time of 10 s. Figure 5 shows that starting from the source to the drain, first the maximum of the electric field appears, followed by the carrier average energy, and finally by the position where the carrier DF demonstrates the most prolonged high-energy tails (calculated with the Monte Carlo method). The consequences of maxima of the AI and $N_{it}(x)$ profiles computed with different realizations of the model correlate with that tendency

the MC-based model for $L_{ch} = 1.2-$ and 2.0 μm transistors, but totally fails for $L_{ch} = 0.5$ μm. The results of this analysis suggest that the simplified DD and ET schemes are not suitable for proper HCD modeling even in the case of long-channel transistors, and thus the exact solution of the BTE is required.
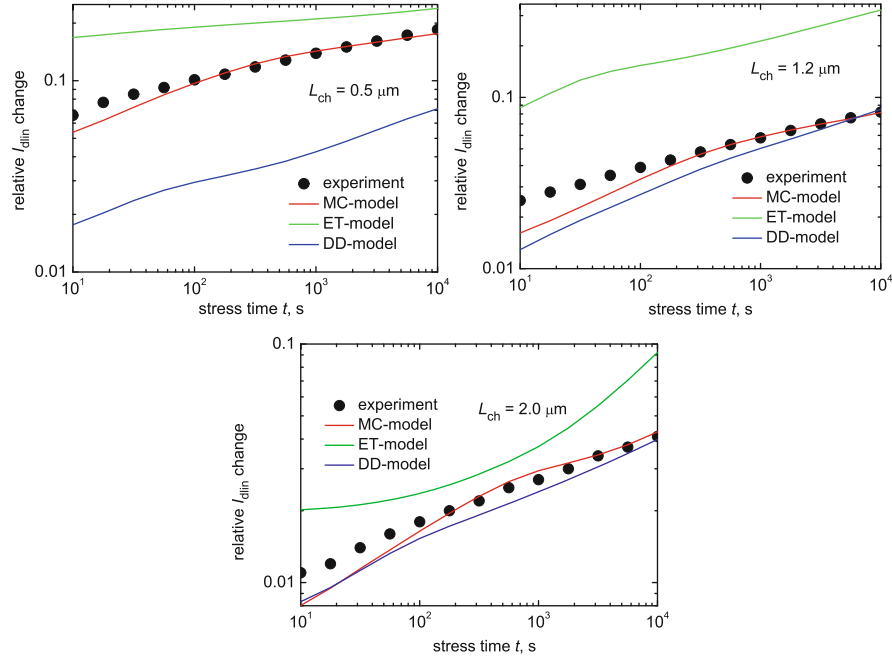
Fig. 25 The linear drain current change $\Delta I_{\mathrm{dlin}}(t)$ obtained with MC-, ET-, and DD-based versions of our HCD model for 0.5-, 1.2-, and 2.0 μm MOSFETs. One can see that the model using the Monte Carlo approach properly represents the experimental data. The model version using the ET scheme dramatically overestimates HCD. If the DD scheme is employed, the model provides good results for $L_{\mathrm{ch}} = 1.2$ and 2.0 μm transistors but totally fails for the 0.5 μm counterpart

4.2 The HCD Model Based on the Deterministic Boltzmann Transport Equation Solver

Although the Monte Carlo method is flexible and allows us to relatively easily incorporate various scattering mechanisms and complicated band structures, it leads to a high computational burden, especially when low statistical noise is required, in order to thoroughly resolve high-energy tails of the carrier DF. Another disadvantage of this method is that although EES can be easily implemented in this method, in practice its consideration further increases the computational costs. Instead, the BTE can be solved deterministically by representing the energy DF as an SHE of an arbitrary order [22, 70–73]. Compared to the Monte Carlo approach, this method requires a substantial amount of memory, not CPU time. Therefore, the amount of RAM available was the limiting factor that prevented practical realization and use of the SHE solver. However, recently even simulations of 3D devices have become possible also on an average workstation [72]. It was also shown that scattering mechanisms (in particular, EES) can easily be included in the SHE method [73]. Another important advantage that can be achieved with the SHE

Fig. 26 The schematic representation of our new HCD model implemented into the deterministic BTE solver ViennaSHE. ViennaSHE allows to reduce the computational burden, incorporate EES important in the case of ultra-scaled devices, and self-consistently consider trap generation processes and scattering mechanisms
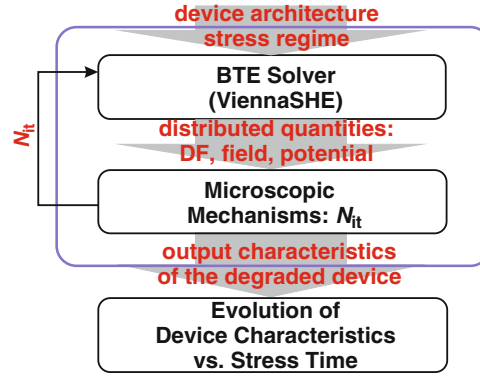
solver as a transport module of our HCD model is that the trap generation processes and scattering mechanisms can be considered self-consistently within the same simulation framework. All of these circumstances make the SHE solver of the BTE attractive for simulations of ultra-scaled MOSFETs, in particular for HCD modeling in these devices. Our new HCD model is implemented in the deterministic BTE solver developed at our institute and named ViennaSHE (see Fig. 26) [20,72,74,75].

In our MC-based model, we considered the SP and MP mechanisms independently, and the resulting concentration of interface traps was evaluated as a superposition of the SP- and MP-induced contributions; cf. (26) This assumption—as well as independent treatment of bond-breakage mechanisms and EES in the Bravaix model [23, 28]—appears physically unreasonable. In fact, the bond dissociation converts the same precursors (passivated Si–H bonds) into the same defects (P_b centers), and therefore, the SP and MP mechanisms are just alternative pathways of the same dissociation reaction. Hence, they need to be considered self-consistently within the same system of the rate equations.

Following the Hess model [7], we consider all possible combinations of bond dissociation events triggered by a solitary hot carrier and by a series of colder carriers (see Fig. 10, right). To avoid mixing with the SP and MP processes that correspond to bond rupture from the ground and last bonded states, we call the process that is induced by a single hot carrier and related to excitation of one of the bonding electrons to anti-bonding state the AB mechanism, while we refer to bond dissociation induced by the multivibrational excitation the MVE mechanism. A superposition of MVE AB mechanisms means that first the bond is excited to an arbitrary level and then hydrogen release is induced within a single collision with a hot electron. Mathematically, this means that the system of rate equations (22) has to be modified in order to include bond-breakage/passivation rates from each level:

$$\frac{\mathrm{d}n_0}{\mathrm{d}t} = P_\mathrm{d}n_1 - P_\mathrm{u}n_0 - R_0 n_0 + P_0 N_\mathrm{it}^2$$

$$\frac{\mathrm{d}n_i}{\mathrm{d}t} = P_\mathrm{d}(n_{i+1} - n_i) - P_\mathrm{u}(n_i - n_{i-1}) - R_i n_i + P_i N_\mathrm{it}^2 \qquad (27)$$

$$\frac{\mathrm{d}n_{N_l}}{\mathrm{d}t} = P_\mathrm{u}n_{N_l-1} - P_\mathrm{d}n_{N_l} - R_{N_l} n_{N_l} + P_{N_l} N_\mathrm{it}^2,$$

where R_i and P_i are the bond-rupture and passivation rates from/to the ith level involved. The former ones are calculated as

$$R_{\mathrm{a},n_i} = w_\mathrm{th}\exp\left[-(E_\mathrm{a} - E_i)/k_\mathrm{B}T\right] + \nu_\mathrm{AB} I_{\mathrm{AB},i}, \qquad (28)$$

where the first Arrhenius term describes the hydrogen thermal excitation from a bonded state to the transport mode (with the corresponding attempt frequency w_th), while the second term represents the contribution of the AB process and is expressed by the AI. However, in this model the AI structure reflects the fact that if dissociation occurs from level i, the potential barrier for hydrogen release is reduced due to the higher-energy position of this state:

$$I_{\mathrm{AB},i} = \int f(E)g(E)\sigma_0(E - E_\mathrm{a} + E_i)^p v(E)\mathrm{d}E. \qquad (29)$$

As for the bond excitation/deexcitation rates $P_\mathrm{u}/P_\mathrm{d}$, they are expressed via the AI for the MVE process in the same manner as in (25).

Similar to the system (22), we solve (27) by applying the timescale hierarchy, and thus the system reduces to the single equation

$$\frac{\mathrm{d}N_\mathrm{it}}{\mathrm{d}t} = (N_0 - N_\mathrm{it})\,\mathfrak{R} - N_\mathrm{it}^2\mathfrak{P}, \qquad (30)$$

where $\mathfrak{R}$ stands for the cumulative bond-breakage rate. This rate is calculated by summation of the rates from each level labeled i weighted with the population factor of this level:

$$\mathfrak{R} = \frac{1}{k}\sum_i R_i \left(\frac{P_\mathrm{u}}{P_\mathrm{d}}\right)^i, \qquad (31)$$

while $\mathfrak{P}$ is the total passivation rate onto each eigenstate. However, without loss of generality, one may represent the $\mathfrak{P}$ rate with the Arrhenius term for thermal activation over a single barrier; that is, $\mathfrak{P} = \nu_\mathrm{p}\exp(-E_\mathrm{pass}/k_\mathrm{B}T_\mathrm{L})$, where ν_p is the attempt rate. The normalization factor k is found to be $k = \sum_i (P_\mathrm{u}/P_\mathrm{d})^i$.

The solution of the system (27) is

$$N_{it}(t) = \frac{\sqrt{\mathfrak{R}^2/4 + N_0\mathfrak{R}\mathfrak{P}}}{\mathfrak{P}} \frac{1 - f(t)}{1 + f(t)} - \frac{\mathfrak{R}}{2\mathfrak{P}},$$

$$f(t) = \frac{\sqrt{\mathfrak{R}^2/4 + N_0\mathfrak{R}\mathfrak{P}} - \mathfrak{R}/2}{\sqrt{\mathfrak{R}^2/4 + N_0\mathfrak{R}\mathfrak{P}} + \mathfrak{R}/2} \times \exp\left(-2t\sqrt{\mathfrak{R}^2/4 + N_0\mathfrak{R}\mathfrak{P}}\right). \tag{32}$$

Note that the bond-breakage energy can be reduced not only due to the barrier lowering when the bond is heated by the MVE process but also due to statistical variations of the activation energy E_a as well as due to the interaction between the oxide electric field and the dipole moment of the bond. The dispersion of the activation energy was observed in electron-spin resonance studies [54] and also in experiments on HCD recovery [55]. In the model, we assume that E_a is a normally distributed quantity with a mean value and standard deviation of 1.5 and 0.15 eV, respectively. These values are in good agreement with experimental ones [54, 55]. We sample the activation energy in the range of $[\langle E_a \rangle - 3\sigma_E; \langle E_a \rangle + 3\sigma_E]$. For each sample value, the AI, the bond-breakage rates, and the interface state density N_{it} are calculated according to (29), (31), and (32), respectively. Then the average concentration N_{it} is produced by integration of N_{it} weighted with the Gaussian distribution over the E_a sampling range.

As for the interaction of the electric field with the dipole moment of the bond, it is modeled in the same fashion as proposed in [49, 76]. The corresponding energy reduction is found as the product of the bond dipole moment and the electric field $d \times E_{ox}$. Note that this interaction was reported to be responsible for two different slopes of the degradation curves calculated experimentally during hot-carrier stress [48, 56] and also affects damage generated during another degradation mode, namely, during bias temperature instability [77].

To validate the model, we used a family of SiON n-MOSFETs with an identical architecture but different channel lengths: 65, 100, and 150 nm. These devices were stressed at their worst-case HCD conditions. We were aware that the transition from long- to short-channel devices (in terms of HCD) occurs in the targeted range of channel lengths (65–150 nm) and therefore measured the substrate current I_{sub} as a function of V_{gs} at a fixed V_{ds} in the MOSFETs with the gate lengths of 100 and 150 nm (the 65-nm counterpart was treated as a short channel device). We have realized that in the 150-nm device, I_{sub} has a maximum at $V_{gs} \sim 0.5V_{ds}$, thereby demonstrating long-channel behavior. As for the 100-nm MOSFET, the I_{sub} maximum corresponds to $V_{gs} \sim 2/3V_{ds}$. Therefore, the device with the gate length of the 65-nm device was stressed at $V_{gs} = V_{ds} = 1.8$ and 2.2 V, the 100-nm transistor at $V_{gs} = 1.2$ V, $V_{ds} = 1.8$ V and $V_{gs} = 1.46$ V, $V_{ds} = 2.2$ V, while the stress voltages for the 150-nm counterpart were $V_{gs} = 0.9$ V, $V_{ds} = 1.8$ V and $V_{gs} = 1.1$ V, $V_{ds} = 2.2$ V. The MOSFETs were subjected to hot-carrier stress for $\sim$8 ks at room temperature.

The devices were stressed at high V_{ds}, and thus the AB mechanism should play a major role. This idea is supported by the carrier energy DFs calculated
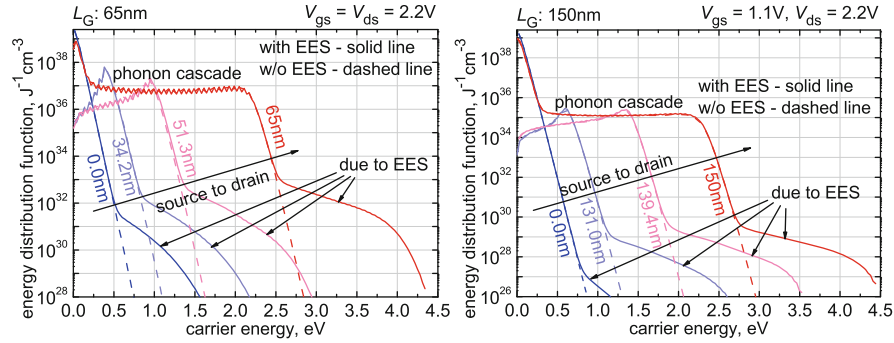
Fig. 27 The carrier DFs calculated using ViennaSHE for the 65- and 150-nm devices stressed at $V_{gs} = V_{ds} = 2.2$ V and $V_{gs} = 1.1$ V, $V_{ds} = 2.2$ V. For comparison, DFs simulated ignoring EES are also presented. EES plays a significant role in populating high-energy tails of the DFs. This results in humps pronounced at high energies. In the entire range of the varying coordinate x, these functions are severely non-equilibrium
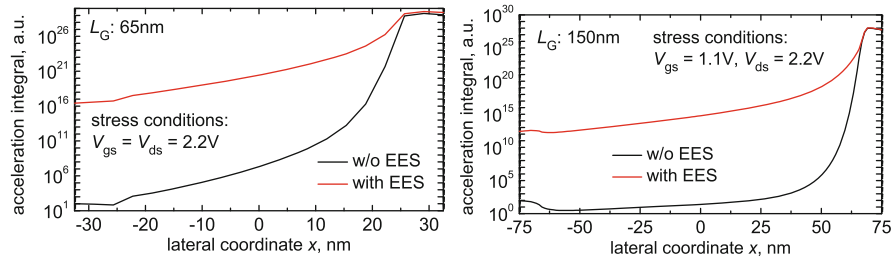
Fig. 28 The AI for the ground state calculated for the devices with gate lengths 65 and 150 nm stressed at $V_{gs} = V_{ds} = 2.2$ V and $V_{gs} = 1.1$ V and $V_{ds} = 2.2$ V. The AIs were evaluated with and without the effect of EES. It can be seen that EES massively increases the acceleration integral, especially in the areas corresponding to colder carriers, that is, in the source area and in the channel center

for the shortest and longest MOSFETs $V_{gs} = V_{ds} = 2.2$ V and $V_{gs} = 1.1$ V, $V_{gs} = 2.2$ V, respectively (Fig. 27). For comparison, DFs obtained ignoring EES are also depicted. Figure 27 shows the DFs evaluated in different positions of the device. One can see that even in the source area, DFs computed without EES are Maxwellian, while considering EES leads to humps pronounced at higher energies even near the source. Distribution functions obtained in the center of the device and near the drain end of the gate are severely nonuniform, and EES substantially populates their high-energy tails. The same tendency is also visible in Fig. 28, which summarizes the carrier AIs plotted as a function of the lateral coordinate x for same devices and for the same stress conditions as Fig. 27.

A series of interface state density profiles $N_{it}(x)$ calculated for the 65-nm device stressed at $V_{gs} = V_{ds} = 1.8$ V for all stress time steps is plotted in Fig. 29. For comparison, we also present the profiles obtained, ignoring one of the model ingredients. The profiles calculated with the "full" model demonstrate a drain
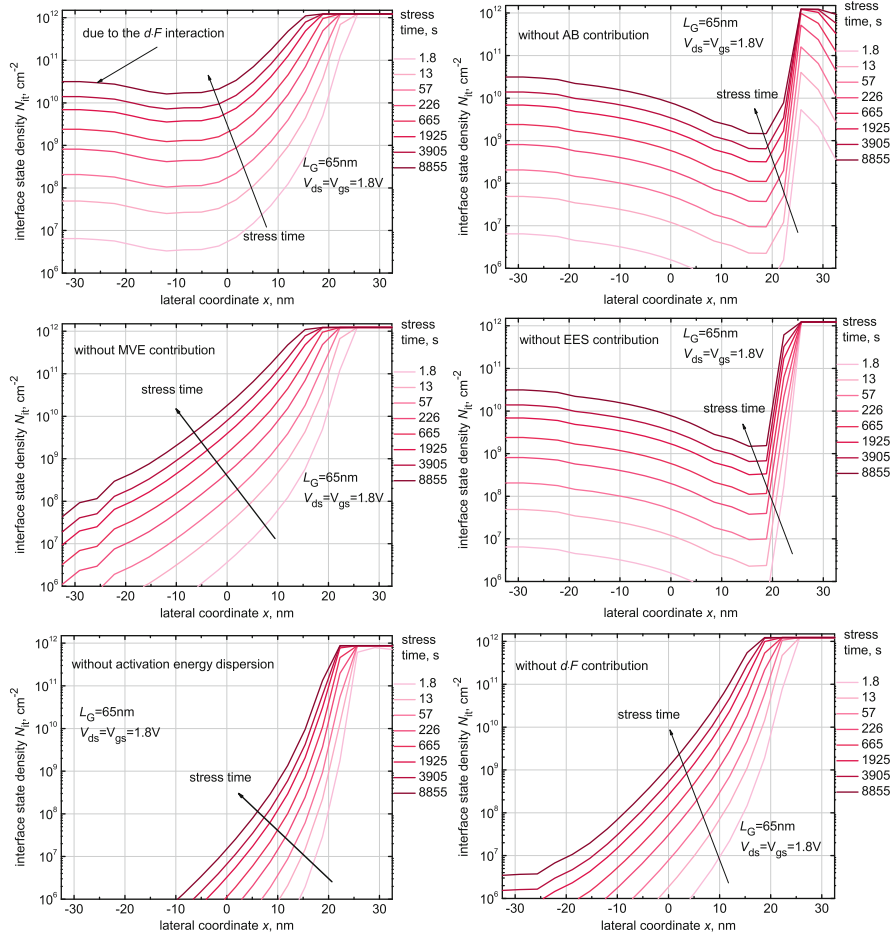
Fig. 29 The interface state density profiles $N_{it}(x)$ ($L_G = 65$ nm, stress voltages: $V_{ds} = V_{gs} = 1.8$ V) calculated using the calibrated model regarding/disregarding one of the essential mechanisms: MVE and AB processes, EES, the dispersion of the activation energy for bond dissociation, and the reduction of this energy due to the interaction between the bond dipole moment and the electric field

maximum. This maximum is related to the contribution of hot electrons that trigger the AB mechanism. Indeed, if we switch off this mechanism in the model, the drain maximum becomes weaker and narrower. At the same time, the $N_{it}(x)$ profiles in the device center and in the drain end of the transistor are not substantially affected. This is because in these device areas, HCD is driven by the MVE mechanism rather than by the AB process. Disregarding EES results in a comparable change of the $N_{it}(x)$ profiles. For instance, the drain maximum also becomes weaker. As we already discussed, EES populates the hot fraction of the carrier ensemble, thereby reinforcing the AB-mechanism. Thus, switching off EES is equal to suppression of the AB-process rate.
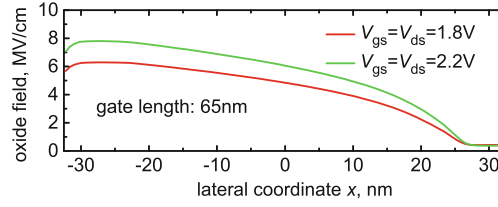
Fig. 30 The interface electric field as a function of the lateral coordinate in the 65-nm n-MOSFET for $V_{gs} = V_{ds} = 1.8$ and 2.2 V. One can see that the field peaks near the source and then monotonously decreases toward the drain

If the MVE mechanism is ignored, this impacts the $N_{it}(x)$ profiles in the transistor center and near the source. The reason is that the carriers are already rather hot in the drain area, and therefore preheating of the bond due to the series of vibrational excitations does not substantially change the bond-breakage rates. In the device section with colder carriers, the AB process is likely only in combination with the MVE-induced bond heating. The effect of the MVE process is screened in the source section due to the energy lowering induced by the interaction of the electric field with the dipole moment of the bond. In all three MOSFETs, the electric field has a maximum near the source. Figure 30 shows the exemplary electric field profile calculated at the interface in the 65-nm MOSFET stressed at $V_{gs} = V_{gs} = 1.8$ and 2.2 V. The electric field peak is pronounced near the source, which corresponds to the strongest activation energy reduction $d \times E_{ox}$. The maximum of the electric field coincides with the secondary maximum observed in $N_{it}(x)$ profiles near the source (see Fig. 29). Note that this maximum disappears when the effect of the $d \times E_{ox}$ energy reduction is neglected. This secondary maximum becomes more pronounced at longer stress times and therefore determines long-term HCD [78]. The effect of the activation energy dispersion is also most prominent in the device section corresponding to cold carriers. Indeed, if carriers are hot enough, they can efficiently dissociate all the available bonds, leading to the saturation of the concentration N_{it} (e.g., near the drain peak), and additional lowering of the bond-breakage energy would not substantially change the situation.

Finally, the model has been calibrated in order to represent the linear drain current degradation measured in all three devices under different stress conditions. It is important to emphasize that the model uses the unique set of the model parameters. Figure 31 shows the experimental $\Delta I_{dlin}(t)$ data plotted vs. the simulated ones as well as those curves obtained disregarding one of the model ingredients. In all six cases, the AB process is crucial; neglecting it results in a severe underestimation of HCD. The same is relevant to ignoring EES, but the effect is weaker than in the case of the AB mechanism. Note also that the role of EES diminishes as we switch from short to longer channels. It is important to emphasize that EES plays a crucial role in the 65- and 100-nm devices and is less important in the 150-nm transistor. Thus, in the case of the 150-nm MOSFET stressed at $V_{gs} = 0.9$ V and $V_{ds} = 1.8$ V, the effect of EES is not pronounced. The EES contribution remains relatively weak
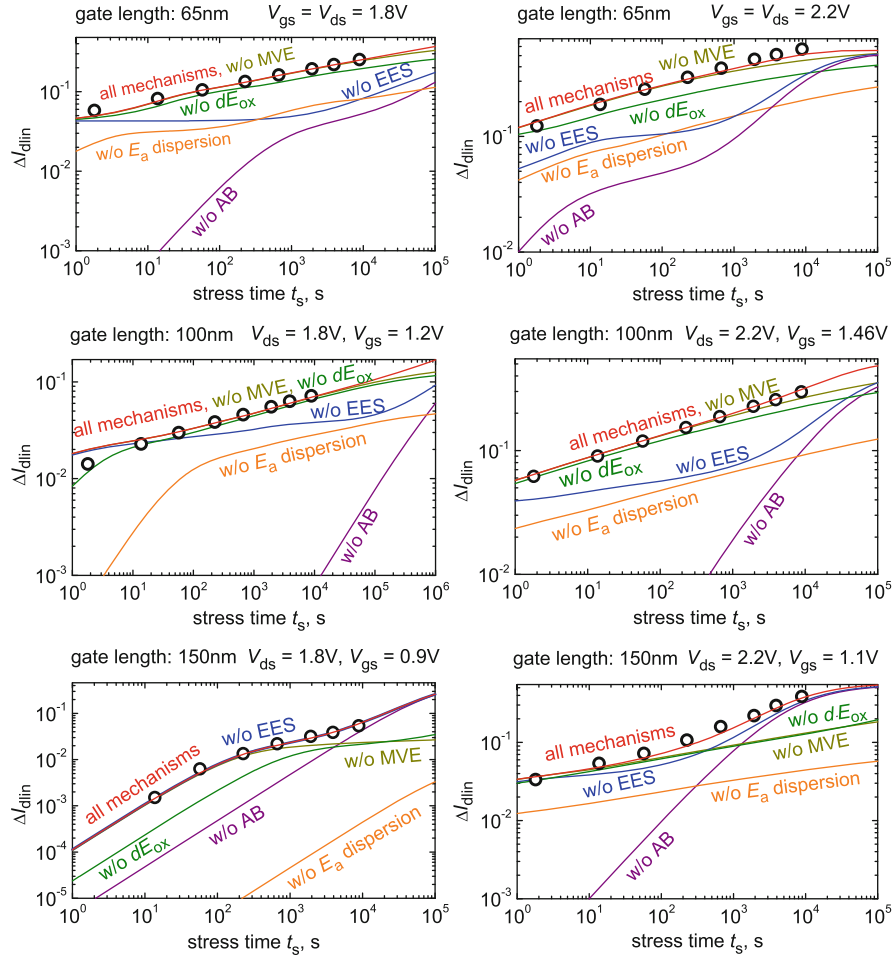
Fig. 31 The relative change of linear drain current ΔI_{dlin} as a function of stress time: experiment (*symbols*) vs. simulations (*lines*) plotted for three different MOSFETs with $L_{\mathrm{G}} = 65$, 100, and 150 nm. Devices were stressed at worst-case conditions at $V_{\mathrm{ds}} = 1.8$ and 2.2 V. The *curves* obtained neglecting one of the model ingredients are plotted for comparison

in the 150 nm device even if the stress voltages are increased to $V_{\mathrm{gs}} = 1.1$ V and $V_{\mathrm{ds}} = 2.2$ V. This finding contradicts the last claims of the Bravaix group [19] but correlates with the idea proposed by Rauch and La Rosa [10, 38] that EES massively strengthens HCD in ultra-scaled devices. The role of the MVE process is not so substantial because under these high-stress voltages, HCD is dominated by the AB mechanism. However, the multiple vibrational excitation of the bond becomes more important at longer stress times [20]. The same is typical also for the interaction of the electric field with the bond dipole moment. For instance, in the 100-nm MOSFET stressed at $V_{\mathrm{gs}} = 1.2$ V and $V_{\mathrm{ds}} = 1.8$ V, the effect of the $d \times E_{\mathrm{ox}}$

energy reduction becomes visible only at $\sim 10^5$ s. Ignoring the energy dispersion shifts all $\Delta I_{\mathrm{dlin}}(t)$ curves toward lower values in all three devices.

Note finally that in contrast to long-channel 5V n-MOSFETs discussed in Sect. 4.2, these shorter n-MOSFETs are characterized with a low hole concentration at the interface, thereby demonstrating unipolar behavior. Therefore, the contribution of holes has a negligibly small effect on HCD.

4.3 Conclusions

We have presented a physics-based model of HCD. The model covers three main aspects of HCD: the carrier transport problem; a microscopic description of the defect creation kinetics; and the degraded device simulations. The transport module provides the link between the microscopic level of defect creation and the simulations of the degraded devices. This module can be realized using either a stochastic or deterministic solver of the BTE. Both solvers have their advantages and shortcomings. For instance, the former employs the Monte Carlo method, which is flexible and allows to easily implement various scattering mechanisms and specific band structures. At the same time, the Monte Carlo method is computationally demanding, and implementation of EES (which is crucial in nanoscale devices) leads to an undesirably long computational time. This circumstance makes the Monte Carlo method not applicable to the modeling of HCD in short-channel MOSFETs. Instead, the deterministic method based on the expansion of the carrier DF into a series of spherical harmonics appears to be more appropriate.

The BTE solver is used to simulate carrier DFs for a particular device architecture and given stress/operating conditions. These functions are then used to calculate the carrier acceleration integral. The AI is the crucial quantity that determines HCD, neither the electric field nor energy deposited by carriers. It controls both main processes responsible for Si–H bond dissociation, namely, the bond-breakage event triggered by a solitary hot carrier and that induced by the multiple vibrational bond excitation due to subsequent bombardments of several colder particles. First, we consider these mechanisms self-consistently as competing pathways of the same bond-breakage reaction. Also, scattering mechanisms (in particular, EES) are incorporated in the same simulation framework and also considered self-consistently with the bond-rupture processes. We want to emphasize that the possibility for such a proper consideration became possible only with the model implemented in the deterministic BTE solver ViennaSHE.

Among EES and voluntary combinations of the AB and MVE mechanisms of bond breakage, there are two important ingredients covered by the model: the dispersion of the Si–H bonding energy and reduction of this energy due to the interaction between the electric field and the bond dipole moment. We have shown that ignoring the former ingredient leads to underestimated HCD, while the latter mechanism determines long-term HCD.

Using the newest version of the model implemented in ViennaSHE, we were able to capture HCD observed in the family of short-channel MOSFETs of an identical architecture but with different gate lengths. It is worth to emphasize that for description HCD in different devices subjected to hot carrier at different voltages, the model uses the unique set of parameters. We have proven the importance of each of the model ingredients. For instance, EES was shown to play the crucial role in the devices with gate lengths of 65 and 100 nm and was less important in the 150 nm MOSFET.

We also have examined the idea of using simplified approaches to solving the BTE by means of DD and ET schemes. These schemes are applicable if the channel length is not shorter than ∼100 nm. Therefore, we used MOSFETs with the channel length of more than 0.5 μm to examine the DD- and ET-based versions of the model. We have demonstrated that both versions are inadequate in order to represent HCD even in the long-channel devices, and the exact solution of the BTE is required.

References

1. E.H. Nicollian, C.N. Berglund, P.F. Schmidt, J.M. Andrews, Electrochemical charging of thermal SiO_2 films by injected electron currents. J. Appl. Phys. **42**(12), 5654–5664 (1971)
2. T.H. Ning, P.W. Cook, R.H. Dennard, C.M. Osburn, S.E. Schuster, H.N. Yu, 1 μm most VLSI technology – Part IV: Hot-electron design constraints. IEEE Trans. Electron Dev. **26**, 346–353 (1979)
3. C. Hu, Lucky electron model for channel hot electron emission, in *Proceedings of the International Electron Devices Meeting (IEDM)*, 1979, pp. 22–25
4. T. Mizuno, A. Toriumi, M. Iwase, M. Takanashi, H. Niiyama, M. Fukmoto, M. Yoshimi, Hot-carrier effects in 0.1 μm gate length CMOS devices, in *Proceedings of the International Electron Devices Meeting (IEDM)*, 1992, pp. 695–698
5. A. Bravaix, C. Guerin, V. Huard, D. Roy, J. Roux, E. Vincent, Hot-carrier acceleration factors for low power management in DC-AC stressed 40nm NMOS node at high temperature, in *Proceedings of the International Reliability Physics Symposium (IRPS)*, 2009, pp. 531–546
6. B. Tuttle, C.G. Van de Walle, Structure, energetics, and vibrational properties of Si–H bond dissociation in silicon. Phys. Rev. B **59**(20), 12884–12889 (1999)
7. W. McMahon, K. Matsuda, J. Lee, K. Hess, J. Lyding, The effects of a multiple carrier model of interface states generation of lifetime extraction for MOSFETs, in *Proceedings of the International Conference on Modelling and Simulation Micro*, vol. 1, 2002, pp. 576–579
8. S. Tyaginov, I. Starkov, H. Enichlmair, J.M. Park, C. Jungemann, T. Grasser, Physics-based hot-carrier degradation models (invited). ECS Trans. **35**(4), 321–352 (2011)
9. P.A. Childs, C.C. Leung, New mechanism of hot carrier generation in very short channel MOSFETs. Electron. Lett. **31**(2), 139–141 (1995)
10. S.E. Rauch, G. La Rosa, F.J. Guarin, Role of E-E scattering in the enhancement of channel hot carrier degradation of deep-submicron NMOSFETs at high V_{gs} conditions. IEEE Trans. Device Mater. Reliab. **1**(2), 113–119 (2001)
11. J.D. Bude, Gate-current by impact ionization feedback in submicron MOSFET technologies, in *Proceedings of the VLSI Symposium on Technical Digest*, 1995, pp. 101–102
12. F. Venturi, E. Sangiorgi, B. Ricco, The impact of voltage scaling on electron heating and device performance of submicrometer MOSFET's. IEEE Trans. Electron Devices **38**(8), 1895–1904 (1991)

13. J.E. Chung, M.C. Jeng, J.E. Moon, P.K. Ko, C. Hu, Low-voltage hot-electron currents and degradation in deep-submicrometer MOSFET's. IEEE Trans. Electron Devices **37**, 1651–1657 (1990)
14. W. McMahon, A. Haggag, K. Hess, Reliability scaling issues for nanoscale devices. IEEE Trans. Nanotechnol. **2**(1), 33–38 (2003)
15. A. Bravaix, V. Huard, Hot-carrier degradation issues in advanced CMOS nodes, in *Proceedings of the European Symposium on Reliability of Electron Devices Failure Physics and Analysis (ESREF), tutorial*, 2010
16. S. Rauch, G. La Rosa, CMOS hot carrier: From physics to end of life projections, and qualification, in *Proceedings of the International Reliability Physics Symposium (IRPS), tutorial*, 2010
17. S.E. Tyaginov, I.A. Starkov, O. Triebl, J. Cervenka, C. Jungemann, S. Carniello, J.M. Park, H. Enichlmail, C. Kernstock, E. Seebacher, R. Minixhofer, H. Ceric, T. Grasser, Interface traps density-of-states as a vital component for hot-carrier degradation modeling. Microelectron. Reliab. **50**, 1267–1272 (2010)
18. Y.M. Randriamihaja, A. Zaka, V. Huard, M. Rafik, D. Rideau, D. Roy, A. Bravaix, P. Palestri, Hot carrier degradation: From defect creation modeling to their impact on NMOS parameters, in *Proceedings of the International Reliability Physics Symposium (IRPS)*, 2012, pp. 1–4
19. Y.M. Randriamihaja, X. Federspiel, V. Huard, A. Bravaix, P. Palestri, New hot carrier degradation modeling reconsidering the role of EES in ultra short n-channel MOSFETs, in *Proceedings of the International Reliability Physics Symposium (IRPS)*, 2013, pp. 1–5
20. S. Tyaginov, M. Bina, J. Franco, D. Osintsev, O. Triebl, B. Kaczer, T. Grasser, Physical modeling of hot-carrier degradation for short- and long-channel MOSFETs, in *Proceedings of the International Reliability Physics Symposium (IRPS)*, 2014 (in press)
21. C. Jungemann, B. Meinerzhagen, *Hierarchical Device Simulation* (Springer, Wien/New York, 2003)
22. S.-M. Hong, A.T. Pham, C. Jungemann, *Deterministic Solvers for the Boltzmann Transport Equation*, Springer edition (Springer, New York, 2011)
23. C. Guerin, V. Huard, A. Bravaix, The energy-driven hot-carrier degradation modes of nMOSFETs. IEEE Trans. Device Mater. Reliab. **7**(2), 225–235 (2007)
24. A. Bravaix, V. Huard, F. Cacho, X. Federspiel, D. Roy et al., Hot-carrier degradation in decananometer CMOS nodes: From an energy driven to a unified current degradation modeling by multiple carrier degradation process, in *Hot-Carrier Degradation*, ed. by T. Grasser (Springer, Wien/New York, 2015)
25. S. Rauch, G. La Rosa, The energy driven paradigm of NMOSFET hot carrier effects, in *Proceedings of the International Reliability Physics Symposium (IRPS)*, 2005
26. S.E. Rauch, G. La Rosa, The energy-driven paradigm of NMOSFET hot-carrier effects. IEEE Trans. Device Mater. Reliab. **5**(4), 701–705 (2005)
27. S. Rauch, F. Guarin, The energy driven hot carrier model , in *Hot-Carrier Degradation*, ed. by T. Grasser (Springer, Wien/New York, 2015)
28. Y.M. Randriamihaja, V. Huard, X. Federspiel, A. Zaka, P. Palestri, D. Rideau, A. Bravaix, Microscopic scale characterization and modeling of transistor degradation under HC stress. Microelectron. Reliab. **52**(11), 2513–2520 (2012)
29. M.G. Ancona, N.S. Saks, D. McCarthy, Lateral disrtribution of hot-carrier-induced interface traps in MOSFET's. IEEE Trans. Electron Devices **35**(12), 221–2228 (1988)
30. Y. Leblebici, S.-M. Kang, Modeling of nMOS transistors for simulation of hot-carrier induced device abd circuit degradation. IEEE Trans. Comput. Aided Des. **11**(2), 235–246 (1992)
31. A. Acovic, G. La Rosa, Y.C. Sun, A review of hot carrier degradation mechanism in MOSFETs. Microelectron. Reliab. **36**(7/8), 845–869 (1996)
32. I.A. Starkov, S.E. Tyaginov, H. Enichlmair, J. Cervenka, Ch. Jungemann, S. Carniello, J.M. Park, H. Ceric, T. Grasser, Hot-carrier degradation caused interface state profile - simulations vs. experiment. J. Vac. Sci. Technol. B **29**(1), 01AB09–1–01AB09–8 (2011)
33. D.J. DiMaria, J.W. Stasiak, Trap creation in silicon dioxide produced by hot electrons. J. Appl. Phys. **65**(6), 2342–2356 (1989)

34. D.J. DiMaria, Defect generation under substrate-hot-electron injection into ultrathin silicon dioxide layers. J. Appl. Phys. **86**(4), 2100–2109 (1999)
35. D.J. DiMaria, J.H. Stathis, Anode hole injection, defect generation, and breakdown in ultrathin silicon dioxide films. J. Appl. Phys. **89**(9), 5015–5024 (2001)
36. I. Starkov, H. Enichlmair, S. Tyaginov, T. Grasser, Analysis of the threshold voltage turn-around effect in high-voltage n-MOSFETs due to hot-carrier stress, in *Proceedings of the International Reliability Physics Symposium (IRPS)*, 2012, 6 pp.
37. K. Hess, L.F. Register, B. Tuttle, J. Lyding, I.C. Kizilyalli, Impact of nanostructure research on conventional solid-state electronics: The giant isotope effect in hydrogen desorption and CMOS lifetime. Phys. E **3**, 1–7 (1998)
38. S.E. Rauch, F.J. Guarin, G. La Rosa, Impact of E-E scattering to the hot carrier degradation of deep submicron NMOSFETs. IEEE Electron Device Lett. **19**(12), 463–465 (1998)
39. E. Li, E. Rosenbaum, J. Tao, G.C.-F. Yeap, M.R. Lin, P. Fang, Hot-carrier effects in nMOSFETs in $0.1\,\mu$m CMOS technology, in *Proceedings of the International Reliability Physics Symposium (IRPS)*, 1999, pp. 253–258
40. C. Lin, S. Biesemans, L.K. Han, K. Houlihan, T. Schiml, K. Schruefer, C. Wann, R. Markhopf, Hot carrier reliability for $0.13\,\mu$m CMOS technology with dual gate oxide thickness, in *Proceedings of the International Electron Devices Meeting (IEDM)*, 2000, 135–138
41. R. Woltjer, A. Hamada, E. Takeda, PMOSFET hot carrier damage: Oxide charge and interface states. Semicond. Sci. Technol. **7**, B581–B584 (1992)
42. F.-C. Hsu, K.-Y. Chu, Temperature dependence of hot-electron induced degradation in MOSFET's, IEEE Electron Device Lett. **5**(5), 148–150 (1984)
43. P.A. Childs, C.C. Leung, A onedimensional solution of the Boltzmann transport equation including eelectron–electron interactions. J. Appl. Phys. **79**(1), 222–227 (1996)
44. B. Ricco, E. Sangiorgi, D. Cantarelli, Low voltage hot-electron effects in short channel MOSFETs, in *Proceedings of the International Electron Devices Meeting (IEDM)*, 1984, pp. 92–95
45. A. Abramo, C. Fiegna, F. Venturi, Hot carrier effects in short MOSFETs at low applied voltages. IEDM Tech. Dig. 301–304 (1995)
46. J.W. Lyding, K. Hess, I.C. Kizilyalli, Reduction of hot electron degradation in metal oxide semiconductor transistors by deuterium processing. Appl. Phys. Lett. **68**(18), 2526–2528 (1996)
47. K. Hess, A. Haggag, W. McMahon, B. Fischer, K. Cheng, J. Lee, L. Lyding, Simulation of Si-SiO$_2$ defect generation in CMOS chips: From atomistic structure to chip failure rates, in *Proceedings of the International Electron Devices Meeting (IEDM)*, 2000, pp. 93–96
48. A. Haggag, W. McMahon, K. Hess, K. Cheng, J. Lee, J. Lyding, High-performance chip reliability from short-time-tests. statistical models for optical interconnect and HCI/TDDB/NBTI deep-submicron transistor failures, in *Proceedings of the International Reliability Physics Symposium (IRPS)*, 2001, pp. 271–279
49. C. Guerin, V. Huard, A. Bravaix, General framework about defect creation at the Si/SiO$_2$ interface. J. Appl. Phys. **105**, 114513–1–114513–12 (2009)
50. B.N.J. Persson, Ph. Avouris, Local bond breaking via STM-induced excitations: The role of temperature. Surf. Sci. **390**(1–3), 45–54 (1997)
51. J.W. Lyding, K. Hess, G.C. Abeln, D.S. Thompson, J.S. Moore, M.C. Hersam, E.T. Foley, J. Lee, S.T. Hwang, H. Choi, Ph. Avouris, I.C. Kizialli, Ultrahigh vacuum-scanning tunneling microscopy nanofabrication and hydrogen/deuterium desorption from silicon surfaces: Implications for complementary metal oxide semiconductor technology. Appl. Surf. Sci. **13-132**, 221–230 (1998)
52. K. Stokbro, C. Thirstrup, M. Sakurai, U. Quaade, B.Y.-K. Hu, F. Perez-Murano, F. Grey, STM-induced hydrogen desorption via a hole resonance. Phys. Rev. Lett. **80**, 2618–2621 (1998)
53. A. Stesmans, Revision of H$_2$ passivation of P$_2$ interface defects in standard (111)Si/SiO$_2$. Appl. Phys. Lett. **68**(19), 2723–2725 (1996)
54. A. Stesmans, Passivation of P$_{b0}$ and P$_{b1}$ interface defects in thermal (100) Si/SiO$_2$ with molecular hydrogen. Appl. Phys. Lett. **68**(15), 2076–2078 (1996)

55. G. Pobegen, S. Tyaginov, M. Nelhiebel, T. Grasser, Observation of normally distributed activation energies for the recovery from hot carrier damage. IEEE Electron Device Lett. **34**(8), 939–941 (2013)
56. K. Hess, A. Haggag, W. McMahon, K. Cheng, J. Lee, J. Lyding, The physics of determining chip reliability. Circuits Devices Mag. 33–38 (2001)
57. O. Penzin, A. Haggag, W. McMahon, E. Lyumkis, K. Hess, MOSFET degradation kinetics and its simulation. IEEE Trans. Electron Devices **50**(6), 1445–1450 (2003)
58. C. Guerin, V. Huard, A. Bravaix, The energy-driven hot carrier degradation modes, in *Proceedings of the International Reliability Physics Symposium (IRPS)*, 2007, pp. 692–693
59. A. Bravaix, V. Huard, D. Goguenheim, E. Vincent, Hot-carrier to cold-carrier device lifetime modeling with temperature for low power 40nm Si-Bulk NMOS and PMOS FETs, in *Proceedings of the International Electron Devices Meeting (IEDM)*, 2011, pp. 622–625
60. S.E. Tyaginov, I.A. Starkov, O. Triebl, J. Cervenka, C. Jungemann, S. Carniello, J.M. Park, H. Enichlmair, M. Karner, Ch. Kernstock, E. Seebacher, R. Minixhofer, H. Ceric, T. Grasser, Hot-carrier degradation modeling using full-band Monte-Carlo simulations, in *Proceedings of the International Symposium on the Physical & Failure Analysis of Integrated Circuits (IPFA)*, 2010
61. S. Tyaginov, I. Starkov, O. Triebl, H. Enichlmair, C. Jungemann, J.M. Park, H. Ceric, T. Grasser, Secondary generated holes as a crucial component for modeling of HC degradation in high-voltage n-MOSFET, in *Proceedings of the International Conference on Simulation of Semiconductor Processes and Devices (SISPAD)*, 2011, pp. 123–126
62. S. Tyaginov, I. Starkov, Ch. Jungemann, H. Enichlmair, J.M. Park, T. Grasser, Impact of the carrier distribution function on hot-carrier degradation modeling, in *Proceedings of the European Solid-State Device Research Conference (ESSDERC)*, 2011, pp. 151–154
63. Institute for Microelectronic, TU Wien, *MiniMOS-NT Device and Circuit Simulator*
64. I. Starkov, H. Enichlmair, S. Tyaginov, T. Grasser, Charge-pumping extraction techniques for hot-carrier induced interface and oxide trap spatial distributions in MOSFETs, in *Proceedings of the International Symposium on the Physical & Failure Analysis of Integrated Circuits (IPFA)*, 2012, pp. 1–6
65. T. Grasser, T.-W. Tang, H. Kosina, S. Selberherr, A review of hydrodynamic and energy-transport models for semiconductor device simulation. Proc. IEEE **91**(2), 251–273 (2003)
66. T. Grasser, C. Jungemann, H. Kosina, B. Meinerzhagen, S. Selberherr, Advanced transport models for sub-micrometer devices, in *Proceedings of the Simulation of Semiconductor Processes and Devices (SISPAD)*, 2004, pp. 1–8
67. A. Zaka, Q. Rafhay, M. Iellina, P. Palestri, R. Clerc, D. Rideau, D. Garetto, J. Singer, G. Pananakakis, C. Tavernier, H. Jaouen, On the accuracy of current TCAD hot carrier injection models in nanoscale devices. Solid State Electron. **54**(12), 1669–1674 (2010)
68. A. Gehring, T. Grasser, H. Kosina, S. Selberherr, Simulation of hot-electron oxide tunneling current based on a non-Maxwellian electron energy distribution function. J. Appl. Phys. **92**(10), 6019–6027 (2002)
69. T. Grasser, H. Kosina, S. Selberherr, Influence of the distribution function shape and the band structure on impact ionization modeling. J. Appl. Phys. **90**(12), 6165–6171 (2001)
70. A. Gnudi, D. Ventura, G. Baccarani, One-dimensional simulation of a bipolar transistor by means of spherical harmonics expansion of the Boltzmann transport equation, in *Proceedings of the Simulation of Semiconductor Devices and Processes (SISDEP)*, vol. 4, 1991, pp. 205–213
71. A. Gnudi, D. Ventura, G. Baccarani, F. Oden, Two-dimensional MOSFET simulations by means of a multidimensional spherical harmonics expansion of the Boltzmann transport equation. Solid State Electron. **36**(4), 575–581 (1993)
72. K. Rupp, T. Grasser, A. Jungel, On the feasibility of spherical harmonics expansions of the Boltzmann transport equation for three-dimensional device geometries, in *Proceedings of the International Electron Devices Meeting (IEDM)*, 2011, pp. 789–792

73. K. Rupp, P. Lagger, T. Grasser, A. Jüngel, Inclusion of carrier-carrier-scattering into arbitrary-order spherical harmonics expansions of the Boltzmann transport equation, in *Proceedings of the International Workshop on Computational Electronics (IWCE)*, 2012, pp. 1–4
74. M. Bina, K. Rupp, S. Tyaginov, O. Triebl, T. Grasser, Modeling of hot carrier degradation using a spherical harmonics expansion of the bipolar Boltzmann transport equation, in *Proceedings of the International Electron Devices Meeting (IEDM)*, 2012, pp. 713–716
75. S. Tyaginov, M. Bina, J. Franco, D. Osintsev, Y. Wimmer, O. Triebl, B. Kaczer, T. Grasser, Essential ingredients for modeling of hot-carrier degradation in ultra-scaled MOSFETs, in *Proceedings of the International Integrated Reliability Workshop (IIRW)*, 2013, pp. 98–101
76. J.W. McPherson, Quantum mechanical treatment of Si-O bond breakage in silica under time dependent dielectric breakdown testing, in *Proceedings of the International Reliability Physics Symposium (IRPS)*, 2007, pp. 209–216
77. V. Huard, M. Denais, C. Parthasarathy, NBTI degradation: From physical mechanisms to modelling. Microelectron. Reliab. **46**(1), 1–23 (2006)
78. S. Tyaginov, M. Bina, J. Franco, Y. Wimmer, D. Osintsev, B. Kaczer, T. Grasser, A predictive physical model for hot-carrier degradation in ultra-scaled MOSFETs, in *Proceedings of the Simulation of Semiconductor Processes and Devices (SISPAD)*, 2014 (submitted)